Life Sciences:
Biostructures and Radiation

The competence of the Institute of Nuclear and Hadron Physics in producing, handling and detecting electromagnetic radiation in a wide photon energy range is the basis of biological research and medical applications. About one half of the ressources of the institute are devoted to this field of research. The work is concentrated onto three main topics:
(i) Studies on structural dynamics of biomolecules by means of infrared radiation;
(ii) Cell radiobiology with soft, quasi-monochromatic X-rays;
(iii) Positron emission tomography (PET) for quality assurance of charged hadron therapy.
Structural dynamics of biomolecules: The analysis of molecular processes that underly biological functions is of prime interest for basic research in the field of life science as well as for the development of new diagnostic and ultimately therapeutical applications in medicine. In the past, biochemical investigations have revealed the chemical pathways that determine the turn over of all essential metabolites. Likewise, the machinery of protein interactions at cell membranes and in the cytosol involved in the perception of extracellular signals which form the basis for cellular communication and regulated gene expression have been characterised in detail. Many proteins that are essential for these processes have been crystallised and their structure analysed by X-ray crystallography from which models on structure function relations have been obtained. The sketched success in the elucidation of biomolecular function was made possible by modern methods in isolation, purification, and detection of cellular components and by the use of modern methods in molecular biology. However, the dissection of the complex biomolecular interactions into tractable entities requires the disruption of the cell. Today, information on the kinetics of individual biomolecular transitions, of entire reaction chains, and on the spatial distribution of macromolecular complexes or metabolites in a single cell or a living higher organism is required. It has become clear that the function of many biomolecules is determined by noncovalent changes, therefore, it cannot be approached by biochemical isolation of reaction intermediates. Here, physical, rather than biochemical approaches are required. The IKH has developed new projects in which its competence in the generation and detection of different types of electromagnetic radiation and their exploitation for spectroscopy and imaging is central for these modern aspects of life sciences. IR-radiation generated by a free-electron-laser (FEL) promises new insight into the structural dynamics of biomolecules. Absorption of IR-radiation is an inherent property of the vibrational modes within proteins, lipids and DNA, thereby, allowing label-free detection of biomolecules. Vibrational frequencies are directly related to molecular structure and their analysis is extremely informative on structural changes during biomolecular function. By this technique we study for example conformational changes in the visual photoreceptor which triggers cellular responses to visible light. Homology with hormone receptors renders this system an interesting model system for molecular pharmacology. To allow a broad application of static and time-resolved IR-absorption measurements exploiting the unique features of IR-FEL radiation, the design of dedicated equipment for the investigation of biomolecules under native conditions is a major activity at the IKH.
Cell radiobiology: This activity is aimed at the determination of the relative biological effectiveness (RBE) of X-rays with photon energy values between 10 and 100 keV for different biological endpoints. Since such photon radiation is widely used in diagnostic and therapeutic radiology, a precise knowledge of RBE values is highly desirable. The investigations will be performed with quasi-monochromatic X-rays delivered by the channeling radiator at the ELBE superconducting electron accelerator. In parallel to the installation of the beam line, the radiobiological methods and the dosimetric techniques established in preparation of the experiments at the ELBE beam, have already been applied to cell irradiation studies at conventional low-energy X-ray sources. For four cell lines the biological endpoints cell death and micronucleus formation (as the indication

of a radiation induced genetic cell defect) have been studied. The results of these experiments revealed that the RBE of X-rays applied for mammographic diagnostics is slightly larger than one; however, the RBE enhancement is not as pronounced as it has been expected from investigations reported in the literature. In a common project with the Institute of Bioinorganic and Radiopharmaceutical Chemistry (IBR) of the FZR the ELBE channeling radiation will be applied to the investigation of a conjectured photon energy dependent RBE due to the accumulation of metallo-organic molecules bearing atoms of high atomic number within radiosensitive structures of cells. These studies are prepared on the one hand by synthesising appropriate compounds in the IBR and on the other hand by Monte Carlo descriptions of local dose enhancement by Auger electrons following the photo electric effect at heavy atoms in the IKH.
Heavy ion therapy: In the framework of the German Heavy Ion Therapy Project the treatment of patients primarily suffering from tumours of the head and neck region has been routinely continued. During three therapeutic beam times of four weeks each at the carbon ion therapy facility of the Gesellschaft für Schwerionenforschung Darmstadt (GSI) 42 patients have been treated in the year 2002. All the therapeutic irradiations have been monitored by means of in-beam PET for quality assurance. The PET data evaluation has been especially focused on locating dose deviations from the treatment plan caused by minor patient mispositioning or by local changes of the tissue density distribution. There are now strong indications that the efforts to install the heavy ion therapy facility at GSI in a highly innovative scientific and technological way (which includes the dose applications by means of intensity controlled raster scanning, the biologically optimised treatment planning and the in-situ PET therapy monitoring) result in successful treatments: For the local control of radioresistant chordomas of the skull base carbon ions are superior to photon irradiations. On this basis the installation of a clinical charged hadron therapy facility at Heidelberg has been decided. Therefore, the physical and technical investigations are directed to a second generation of in-beam PET scanners for this facility. This comprises the development of suitable photon detectors, the construction of a PET-gantry which can be combined with a rotating beam delivery, new PET data acquisition methods for rapidly fluctuating photon fluxes, refined tomographic reconstruction methods and the extension of the PET method from carbon to other ion species.

Structural dynamics of biomolecules

- *Rockefeller University, New York*
- *Universität Orenburg*
- *MPI für Physik Komplexer Systeme, Dresden*
- *MPI für Festkörperphysik, Stuttgart*
- *ENEA, Frascati (Italien)*
- *CLIO, Paris (Frankreich)*

Cell radiobiology

- *Klinik für Strahlentherapie und Radioonkologie, TU Dresden*
- *Institut für Strahlenschutzphysik, TU Dresden*
- *Institut für Bioanorganische und Radiopharmazeuthische Chemie(FZ Rossendorf)*

Heavy ion tumour therapy

- *GSI Darmstadt*
- *Radiologische Klinik der Universität Heidelberg*
- *Deutsches Krebsforschungszentrum Heidelberg*
- *Institut für Bioanorganische und Radiopharmazeuthische Chemie(FZ Rossendorf)*
- *Soltan Institute for Nuclear Studies, Otwock-Swierk, Poland*
- *National Institute of Radiological Sciences, Chiba, Japan*

Installation of Biochemical and Biophysical Working Facilities at the IKH

K. Fahmy

The start of novel experimental activities in the area of life sciences has made necessary the installation of new working facilities for biochemical and biophysical manipulations and preparation of biological samples. For this purpose, a laboratory has been established in close proximity to the ELBE building and has been equipped with a dark working place for preparation of light-sensitive samples such as the visual photoreceptor rhodopsin, or inorganic metal-containing solutions used for metal cluster formation. In addition a routine FTIR spectrophotometer has been set up allowing extensive vibrational characterisation of biosamples that are to be used in FEL applications. Time-resolved spectra in the ms time range from flash lamp-induced reactions can be obtained in house. Equipment for the preparation of monomolecular biofilms and their investigation by Brewster angle microscopy has also been brought to operation. Finally a biochemical bench including the supply with standard laboratory gases has been installed. This allows in place biochemical operations and immediate use of thus prepared samples for spectroscopic, microscopic, and FEL applications. Thus, experiments using advanced spectroscopic equipment for the study of biomolecular structure function relations in life science can now be performed in house. The following sections describe the focus of our works on structural dynamics of biomolecules, where these new facilities have been used extensively.

Fig. 1a

Fig. 1b

Fig. 1c

Fig. 1 *Facilities for biochemical and biophysical manipulations.*
a. *Biochemical work bench for sample preparation.*
b. *Routine FTIR spectrophotometer in dark working place allowing static and time-resolved characterisation of the IR-absorption of samples to be used in IR-FEL applications.*
c. *Film balance and Brewster angle microscope for the analysis of lipidic monolayers.*

Whole Cell Characterisation by Second-Derivative FTIR Spectroscopy for the Detection of Radiation Damage

A. Panteleeva, O. Savchuk, K. Fahmy

Radiation-induced damage of cultured cells serves as a model system for the characterisation and prediction of radiation effects in higher organisms. Several chemical changes in the cell's constituents linked to radiation-induced processes such as radical formation, direct and indirect DNA modification, lipid oxidation and others alter the chemical structure of certain biomolecules. Therefore, label-free detection of these alteration in whole cells is a promising way to reveal radiation effects. This approach requires monitoring of an intrinsic physical property that is related to chemical composition and biomolecular structure. The frequency of molecular vibrations in the mid infrared range (5-10 μm, corresponding to 2000-1000 cm^{-1}) are determined by the atomic masses and force constants of chemical bonds connecting the vibrating nuclei. This gives rise to absorption frequencies which are characteristic of the local chemical constituents in macromolecules(group frequencies). Additional factors such as intermolecular forces further affect the exact frequency, thereby providing a sensitive measure of chemical alterations in multicomponent systems. We have applied IR-spectroscopy to identify mid infrared absorption bands of whole cells that correlate with radiation-induced damage. Lethal and sublethal doses of UV-radiation have been applied to cells cultured in the ELBE cell culture lab. The IR measurement requires detection of very small absorption differences on a large absorption background. Therefore, Fourier transform IR spectroscopy was used to record high signal to noise spectra of whole cells. A cell preparation protocol has been established that allows reproducible mid infrared absorption measurements of irradiated and subsequently dried cells as well as of control cells. To resolve small absorption bands in the total absorption and to exclude artifacts from baseline drifts, second derivative spectra were evaluated. Figure 1 shows 2^{nd} spectra of cells that were measured different times after sample preparation, thus exhibiting increasing contribution from non-specific oxidative reaction products. In contrast to the normal absorption spectrum (Fig. 2) the structure underlying the amide I band is clearly resolved. We have compared the alterations by non-specific oxidative processes with UV-induced spectral changes. Thereby, absorption peaks have been identified that correlate with exposure of the cells to UV-radiation. Absorption differences in the 1700 to 1800 cm^{-1} range indicate formation of oxidised reaction products after increasing UV irradiation.Changes in the amide I range at 1658 cm^{-1} suggest altered protein secondary structure in non-specifically oxidised cells. In irradiated versus normal cells, protein structure is not altered. This indicates that radiation-induced oxidative affect primarily lipids and DNA, whereas non-specific oxidation additional affects proteins. The data evidence that FTIR 2^{nd} derivative spectroscopy provides a sensitive and reproducible measure of radiation-induced chemical modifications in whole cells.

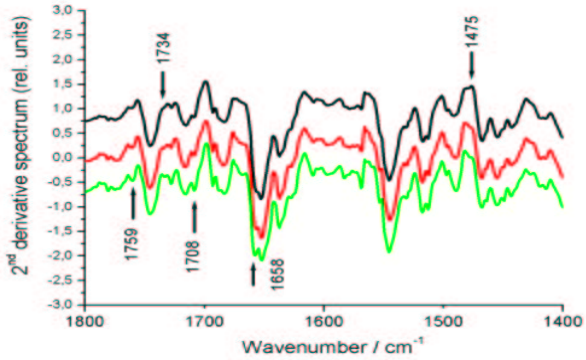

Fig. 1 *2^{nd} derivative FTIR spectra of NIH / 3T3 mouse fibroblast cells. Cells where cultured in DMEM 10 % FCS. UVC irradiation was at 254 nm (2x15W) in petri dishes through 400 μm polypropylene film. For FTIR analysis cells where centrifuged in 0.9 % NaCl solution and the pellet resuspended in the same solution at 10000 cells/μl. Spectra from top to bottom: non-irradiated cells measured 0,2, and 48h after sample preparation At the indicated frequencies, non-specific oxidative processes cause absorption changes over time. Effects of UVC at these positions have been observed for NIH/ 3T3 cells as well as for mammary epithelial cells (MCF12).*

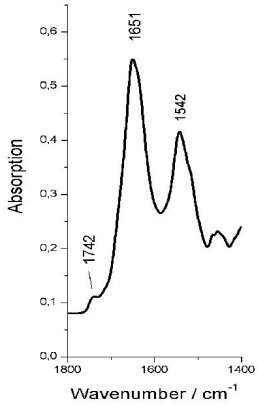

Fig. 2 *Absorption spectrum of whole cells dried on ZnSe. Band structures resolved in the 2^{nd} derivative spectrum are barely visible in the raw data. Likewise, small differences between different passages of the same cell line not visible in the absolute spectrum become resolved in the 2^{nd} derivative spectrum. Corresponding changes can be of the same size as those induced by UV-radiation. Therefore, non-irradiated controls have to be taken from identical passages treated in the same manner as the irradiated samples.*

Analysis of Structural Flexibility in S-Layer Proteins from *Bacillus Sphaericus*

O. Savchuk, J. Raff[1], S. Selenska-Pobell[1], K. Fahmy

Crystalline bacterial surface layers (S-layers) are formed by self-assembling of S-layer proteins. These proteins retain their ability to crystallise in two dimensions after isolation from bacterial cells. Such arrays may serve as attractive templates for the formation of nanostructured surfaces with a repeating pattern of defined physicochemical properties. This approach is based on the ability of S-layer proteins to bind metal cations which may serve as initiation sites for the formation of metal nanoclusters. Metal binding by S-layers is also the basis for approaches to bioremediation using S-layer proteins to adsorb uranium complexes from contaminated solutions. In these biotechnological applications it is necessary to characterise the structural and functional features of S-layer proteins on a molecular and, where possible, on an atomic level in order to optimise desired features through genetic engineering. We have designed and constructed equipment to allow the real time- monitoring of exchange processes occurring between suspensions of S-layer proteins and aqueous solutions of defined compositions. The pH-sensitivity of the secondary structure of isolated S-layers from two strains of *Bacillus sphaericus* has thus been investigated in collaboration with the Radiochemistry Department of the FZR. Using attenuated total reflection FTIR-spectroscopy, mid infrared spectra were recorded in aqueous suspension. This is possible, because the penetration depth of the IR beam is restricted to the μm range without the need of mechanical realisation of μm-sized optical path lengths (see formula 1). As the IR-measuring beam does not transmit the sample, this geometry allows to perform dialysis experiments during spectral recordings. The S-layer proteins from both strands exhibit mainly β-sheet secondary structure as indicated by the amide I (C=O stretching) absorption peak at 1632 cm^{-1}. Decrease in pH induces a frequency upshift of the amide I absorption arguing for the formation of helical or unordered structures. These results demonstrate that S-layer proteins can exhibit structural flexibility. This has to be taken into account for the further development of S-layer-based technical applications and may itself be exploited. Additionally, the data reveal different structural stability against acid denaturation in the two strains. JGA-12 exhibits faster denaturation than the reference strain NCTC-9602.

The secondary structure of the S-Layer of both strains was further analysed by spectral decomposition of the amide I modes. Using band fitting routines, a minimal number of four spectral components in the amide I range was determined (Fig. 2). Their pH dependence strongly supports the acidification-dependent relative decrease in β-structure. The integrated intensity of the fitted component at 1632 cm^{-1} (corresponding to β-sheet) relative to that of the 1640-1660 cm^{-1} absorption is 1.5 and 1.2 at pH 5.7 and 2.0, respectively.

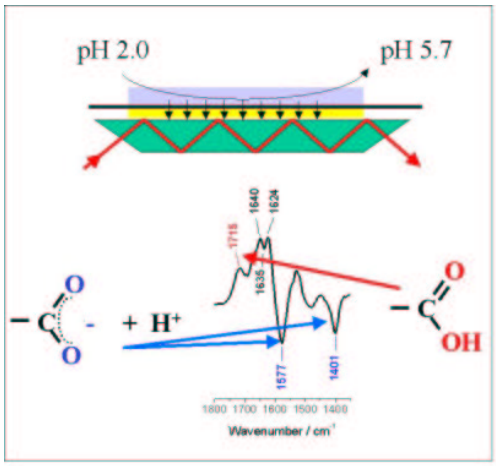

Fig.1 *Attenuated total reflection FTIR-spectroscopy of the pH-induced conformational changes in S-Layer proteins from Bacillus sphaericus. Top: Experimental setup of ATR-cell, allowing dialysis of protons into the sample volume. Absorption changes are detected by attenuation of the IR-beam which is reflected in the ATR crystal(ZnSe). The penetration depth of the electric field amplitude in the rarer medium decays exponentially with the distance z from the crystal surface according to*

$E = E_0 e^{-z/d}$, *with* $d = \lambda_{n1}/2\pi(sin^2\gamma - (n_2/n_1)^2)^{1/2}$

where λ is the wavelength of the IR radiation, n_1 and n_2 are the refractive indices of the IRE and the sample, respectively, and γ is the angle between the surface normal and the IR beam.

Bottom: *Acidification not only causes protonation of carboxylic acids (increase of C=O stretching absorption, decrease of COO- absorption) but also changes of the mainly β-sheet structure of the S-layer as evidenced by the absorption changes around 1620-1640 cm^{-1}.*

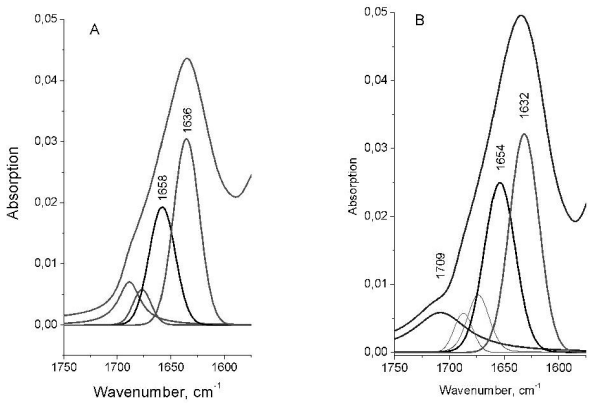

Fig.2 *Amide I band analysis of B sphaericus strain JGA-12. A) Absorption spectrum at pH 5.7 Major contributions to the amide I absorption are found at 1658 and 1636 cm^{-1} indicative of helial and β-sheet structure, respectively. B) Absorption spectrum at pH 5.7. The increased relative intensity of the 1654 cm^{-1} band indicates proton-induced formation of random or helical structures. The broad absorption at 1709 cm^{-1} corresponds to the carbonyl stretching mode of prtonated carboxylic acids (Glu and Asp side chains). Bands between 1675 and 1700cm^{-1} are indicative of β-turns.*

[1] *FZR, Institute of Radiochemistry*

Investigation of Structure and Function of the Visual Photoreceptor Rhodopsin [D]

N. Lehmann, T.P. Sakmar[1], K. Fahmy

G-protein-coupled receptors (GPCRs) play a central role in diverse cellular signalling cascades mediating the action of hormones, neurotransmitters, and odours. They are heptahelical transmembrane proteins that bind extracellular ligands and respond with conformational changes that alter their intracellular surface. This change in surface structure is recognised by cellular guanosine nucleotide-binding proteins (G-proteins) which release bound guanosinediphosphate (GDP) and take up the corresponding triphosphate GTP. We study structure function relationships in bovine rhodopsin, a vertebrate photoreceptor. Although activated through light absorption by covalently bound 11-cis retinal, this systems shares many similarities with other GPCRs. We have used FTIR difference spectroscopy to monitor structural changes during photoactivation. This technique compares the IR-absorption after photoactivation with that in the dark. The difference spectrum contains information only on those chemical groups that have undergone specific light-induced structural or physical changes. Absorption by the large majority of amino acids and peptide backbone vibrations that are not involved in conformational changes vanish in the difference spectrum. It is of special importance to elucidate structural changes in the cytoplasmic surface of the membrane protein. Our previous ATR-FTIR studies have revealed protonation changes during rhodopsin transducin interactions (Fig. 1). We have now started to investigate interaction domains using biochemical modifications of the rhodopsin surface and synthetic peptides from exposed protein regions (Fig. 2).

Fig. 1 *Proposed mutual orientation of rhodopsin (green) and transducin. After photoisomerisation of 11-cis retinal (red space-filling representation) the cytosolic conformation (upper part of the molecule) changes and interacts with transducin, the G-protein in photoreceptor rod cells. The Interaction site at Glu*^{134} *has been suggested by earlier FTIR investigations [1,2].*

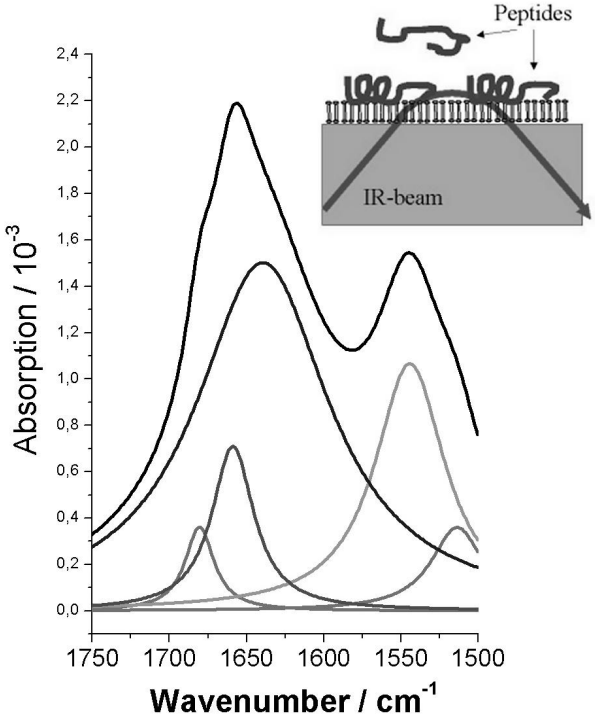

Fig. 2 *The folding capacity of peptides corresponding to residues 310 to 321 in helix 8 of rhodopsin, i.e. the small carboxyl-terminal stretch running vertical the transmembrane helices, has been investigated. The native sequence partially adopts a helical structure on the surface of liposomes. This is deduced from the amide I absorption maximum at 1656 cm*$^{-1}$*. The component bands have been determined by fitting the measured curved (top). A scrambled sequence of identical length and amino acid composition does not show the helical component. The native helix 8, which is involved in transducin recognition, may thus constitute an independently folding receptor domain. The inset shows how the spectra were obtained by ATR-FTIR difference spectroscopy. In this geometry, the absorption by the lipid-binding fraction of peptides is specifically enhanced over the non-binding fraction.*

[1] K. Fahmy; Binding of transducin and transducin-derived peptides to rhodopsin studied by attenuated total reflection-Fourier transform infrared difference spectroscopy;q Biophys. J. 75 (1998) 1306-1318

[2] K. Fahmy, T.P. Sakmar, and F. Siebert; Transducin-dependent protonation of glutamic acid 134 in rhodopsin; Biochemistry 39 (2000) 10607-10612

[1] *Rockefeller, University New York, New York, USA*

Analysis of Dye DNA Interactions

O. Savchuk, K. Fahmy

With the deciphering of the human genome, direct targeting of DNA has become a major challenge in drug research. Expression of specific genes related to disease may be inhibited if drugs can specifically recognise and possibly destroy undesired genomic information. This may be done by direct chemical attack or indirectly by site-specific generation of reactive singlet oxygen species. The latter is achieved in photodynamic therapy, which in combination with DNA-binding ligands, may increase directed DNA damage. Likewise, directed destruction of DNA is required in therapeutic approaches against cancer. Radiotherapy may particularly profit from a gain in DNA damage, when the site of radical formation is in close proximity of the target DNA. In this case DNA-binding ligands that carry covalently bound metals as efficient X-ray absorbers are promising substances to be optimised for therapy. Different dyes such as Rhodamine 6G, acridine and methylene blue can be used as the energy-transferring groups for the creation of specific changes (modification, cleavage) of the DNA backbone. IR has proven useful as a non-destructive, highly sensitive method to detect conformational changes in biomolecules. We have designed and carried out preliminary experiments that use FTIR spectroscopy to detect ligand binding events in DNA. Several intercalating and non-intercalating dyes are used as test substances for the detection of vibrational modes that can be used as monitors for drug DNA interactions. Thereby, the kinetics of reassociation of thermally dissociated ligand DNA complexes can be followed in real time by reappearance of vibrational modes typical of the complex. Binding of rhodamine has thus been shown to be accompanied by changes in the asymmetric PO_2- stretching modes around 1220 cm^{-1} of the phosphate sugar backbone. This agrees with the expected interaction of the positive charges of amino groups of rhodamine with the negatively charged DNA backbone. The experiments establish the basis for a comprehensive study of DNA structural dynamics by FEL IR-pump probe experiments. Observing the formation and disruption of the electrostatic interactions will provide fundamental as well as application-oriented knowledge on DNA ligand binding.

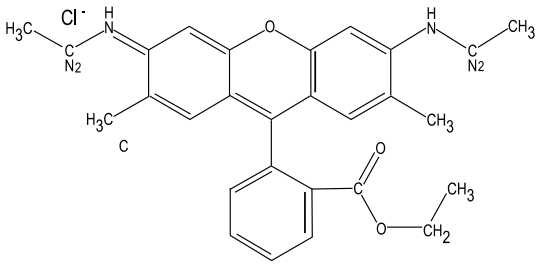

Fig. 1 *Structure of rhodamine 6G used as a DNA-binding ligand in the IR-based label-free investigation of DNA-ligand interactions.*

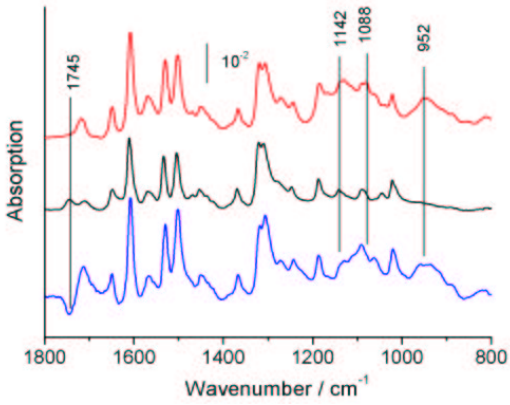

Fig. 2 *IR absorption spectra of rhodamine. In the pure compound (middle), the C=O stretching mode of the acetyl ester between 1700 and 1800 cm_{-1} is split in two frequencies, indicating populations with strong and low H-bonding. In the presence of DNA (molar ratio 1:10, top; 1:1, bottom) a single C=O stretch is observed at an intermediate frequency, indicative of the formation of a single DNA-binding population of rhodamine molecules. Additional differences are seen in the 1100-1200 cm^{-1} range of the symmetric PO_2- stretching modes of DNA, evidencing the interaction of rhodamine with the DNA backbone.*

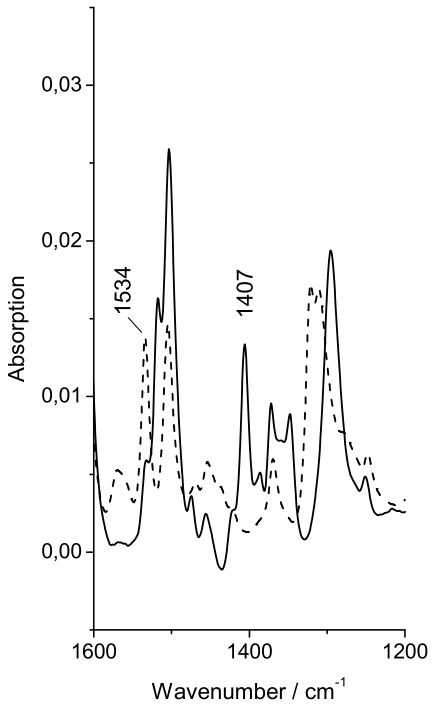

Fig. 3 *Comparison of the IR absorption of rhodamine 6G in H_2O and D_2O. The predominant effect of H/D exchange is the shift of the intense absorption at 1534 cm^{-1} to 1407 cm^{-1}. Therefore, we assign this band to the N-H and N-D bending vibrations of rhodamine, respectively.*

Experimental Set-Up for IR Measurements of Dynamics of Water-Lipid Interaction

G.I. Furlinski, K. Fahmy

Biomembranes are crucial to the life of the cell. Despite their differing functions, all biological membranes have a common general structure: each is a very thin film of lipid and protein molecules, held together mainly by noncovalent interactions. Cell membranes are dynamic, fluid structures, and most of their molecules are able to move about in plane of the membrane. The lipid molecules are arranged as a continuous double layer about 5nm thick.

Lipids constitute about 50% of the mass of most animal cell membranes, nearly all of the remainder being proteins. There are approximately 5x10^6 lipid molecules in a 1μm x 1μm area of lipid bilayer [1]. All of the lipid molecules are amphipathic - that is, they have a hydrophilic or polar end (head) and a hydrophobic or nonpolar end (tail).

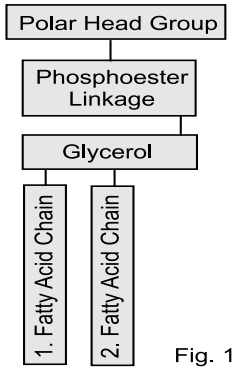

Fig. 1

The most abundant membrane lipids are the phospholipids (Fig. 1). These have a polar head group and two hydrophobic hydrocarbon tails. The tails are usually fatty acids, and they can differ in length (they normally contain between 14 and 24 carbon atoms).

One of the most important properties of the lipid bilayer is its fluidity, which is crucial to many membrane functions. Fluidity allows lipid molecules are able to diffuse freely within lipid bilayers. Our goal is to excite vibration levels of the hydrogen bonds between phosphate groups and water molecules and find their relaxation time by pump-probe experiments. In other words, we want to monitore the dynamics of water-lipid interaction. The experiments will be implemented with two types of lipid molecules - phosphatidylcholine and phosphatidylserine. For this purpose an experimental set-up shown in Fig. 2 has been designed. The system is compact and movable. The last feature is important, because experiments with two different laser sources are planned. The two tuneable sources are a femtosecond laser system equipped with a wavelength converter system "TOPAS" and a Free electron laser (FEL).

The femtosecond system after the wavelength converter, covers 2.8μm - 18μm spectral region with 1kHz repetition rate and energy from 0.2μJ to 2.5μJ. With a pulse duration of about 60fs, it allows to measure in the femtosecond and subpicosecond time scale.

The FEL, which will be tunable in the mid- and far-IR regions with pulses from 0.5ps up to several picoseconds, will allow to measure in the picosecond and nanosecond time scale. Our experimental set-up is based on InfraRed Reflection-Absorption Spectroscopy (IRRAS). This technique allows to measure the chemical composition and conformation of the lipid monolayer and its conformational changes. A comprehensive description of this method is found in the review paper by Gericke et al [2].

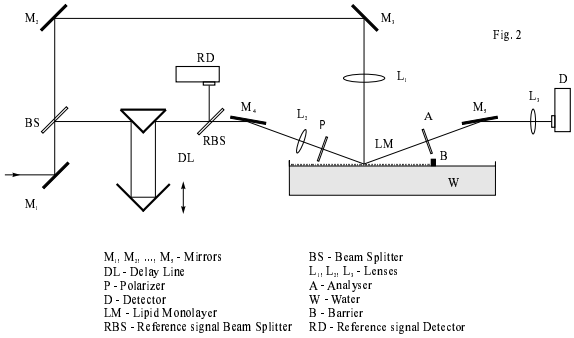

It describes the theoretical models and results for reflection coefficients in three-layer systems consisting of a transparent, isotropic, semi-infinite, incidence medium; an absorbing, anisotropic uniaxial homogeneous film; and an absorbing, isotropic uniaxial homogeneous film; and an absorbing, isotropic, semi-infinite substrate. Below we present some requirements for the experimental setup, generalising experimental experience with IRRAS.

Because the state of the monolayer is strongly affected by impurities, the setup should be completely enclosed. For experiments to determine transition dipole moment directions, an optical setup with flat mirrors (or at least curved mirrors with a long focal length) to direct the IR beam onto the water surface is necessary.

To determine transition dipole moment directions with reasonable accuracy close to the Brewster angle, high efficiency of the polarizer (at least 99%) is essential. Due to the low intensity of the light reflected from water, MCT detectors are necessary.

Compensation of the water vapour rotation-vibration bands is necessary. Three different experimental approaches have been developed to overcome the problem of water vapour.

- the bands may be effectively compensated by accurately regulating the humidity in the sample compartment with help of an adjustable very low flow of dry nitrogen in the chamber.
- the Langmuir trough must be designed with miniaturised surface film sample well and reference well.
- a combination of these two methods along with substitution D_2O for H_2O in the subphase may provide additional advantages.

[1] B. Alberts, A. Johnson, J. Lewis, M. Raff, K. Roberts, P. Walter, The Cell, Garland Science, (2002)
[2] R. Mendelson, J. W. Brauner, and A. Gericke, Ann. Rev. Phys. Chem., 46 (1995) 305-334

Infrared Characterization of Environmental Samples by Pulsed Photo-Thermal Spectroscopy

H. Foerstendorf[1], W. Seidel, K.H. Heise[1], R. Nicolai[1], A. Schamlott[2], J.M. Ortega[3], F. Glotin[3], R. Prazeres[3]

The low metal concentration in environmental samples often limits the interpretation of results of studies investigating the interaction processes between metal ions and environmental compartments by vibrational spectroscopy. The aim of this investigation is to reduce the limits for IR-spectroscopic analyses and to develop in situ methods for environmental samples. For this purpose the photo-thermal infrared spectroscopy of different concentrations of solid neodymium nitrate ($Nd(NO_3)_3 6H_2O$) dissolved in a potassium bromide (KBr) matrix serving as a model system was used.

The photo-thermal detection method is based on a thermo-elastic deformation bump generated by intermittent laser heating and thermal expansion [1]. A solid sample is irradiated by a modulated beam of monochromatic light produced by a tuneable free electron laser (FEL) and a probe beam (e.g. HeNe laser) which is reflected from the sample. Depending on the modulated intensity of the pump beam the photoinduced displacement of the probe beam changes periodically and thus a different reflection angle is observed (Fig. 1). At first order the thermal beam deflection (TBD) is proportional to the absorption coefficient of the material under investigation, thus providing direct access to acquisition of absorption spectra. The detection limit is expected to be extremely low since absorptions as low as 10^{-6} to 10^{-8} have been measured in the visible region by this method [2].

The spectra were recorded within a small spectral range where narrow bands show up. The observed spectral features can be assigned to vibrational modes of the nitrate anion. A comparison of the spectra recorded with FTIR and TBD spectroscopy show a good agreement for the high and middle salt concentration (Fig. 2B,C). whereas spectral deviations are observed at low concentration (Fig. 2A).

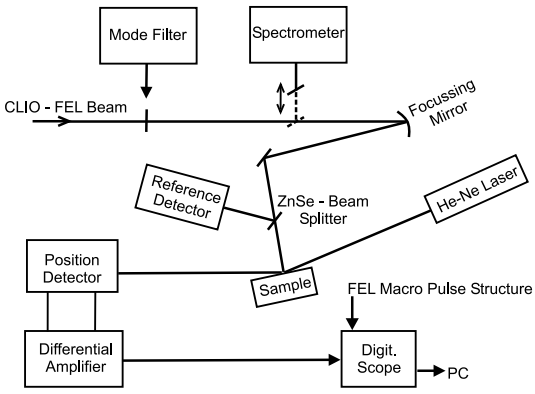

Fig. 1 *Schematic diagram of the thermal deflection experiment setup, at CLIO FEL in Orsay/France.*

From these spectra it appears that the deflection method is more efficient to detect low amounts of substance than conventional FTIR spectroscopy, since weak bands around 815 and 743 cm^{-1} are clearly observed in the FEL spectra which are hardly present in the respective FTIR spectra due to the low concentration. Furthermore, in contrast to transmission FTIR spectroscopy only a small fraction of the sample is detected in the TBD experiment. Therefore, the high quality of the photo-thermal spectra presented here emphasises the high detection efficiency of this acquisition technique [3].

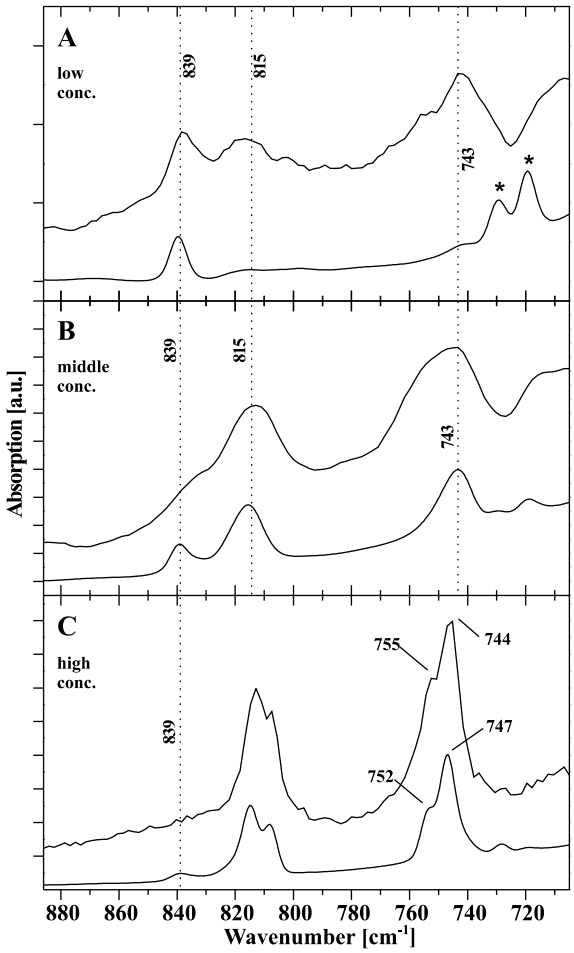

Fig. 2 *Photo-thermal (upper traces) and FT-IR (lower traces) spectra of $Nd(NO_3)_3 \cdot 6H_2O$ in KBr matrix (300 mg) at different concentrations. Low conc.: 0.08 mg; 0.6 mM (A). Medium conc.: 0.3 mg; ∼2 mM (B). High conc.: 0.7 mg; ∼5 mM (C). Bands representing impurities of the KBr matrix are indicated by ⋆(A).*

[1] M.A. Olmstead et al., Appl. Phys. A32 (1983) 144
[2] A. Mandelis, Physics Today, (Aug. 2000) 29
[3] W. Seidel et al., (submitted to Eur. Phys. J. - Applied Physics)

[1] *FZR, Institute of Radiochemistry*
[2] *FZR, Radiation Source ELBE*
[3] *LURE, Université de Paris-Sud, Orsay, France*

Using Pulsed Photo-Thermal Spectroscopy for Microspectroscopy in the Infrared Region. A First Approach

W. Seidel, H. Foerstendorf[1], K.H. Heise[1], J.M. Ortega[2], F. Glotin[2], R. Prazeres[2]

Photo-thermal spectroscopy using a pulsed pump source potentially provides spatial information of a sample surface. This may result in a microspectrometric technique for determining the distribution of metal species on mineral surfaces. The border range between an implanted and an untreated region of the surface of a germanium substrate was investigated by photo-thermal spectroscopy. The substrate was implanted by oxygen ions (O^+) which were restricted to a distinct region of the substrate by partially covering the surface with a metal plate during the implantation process. This substrate serves as a model system for future investigations of mineral surfaces.

We have used this method in order to take advantage of the pulsed character of the infrared laser. The incident energy is deposited in a short time. The heat generation will exhibit a corresponding time dependence, its time constant being of the order of the lifetime of the excited level (ps to ns). A temperature profile then develops in the sample via heat diffusion which can be described by a thermal diffusion length which was found in the μm range for solid states [1,2]. Let us assume that the optical absorption is due to a small defect: Therefore, if one measures the induced deflection with a sufficiently small laser probe, the signal will be found only in the vicinity of this defect within one thermal diffusion length. With a probe beam having a small spot diameter one can hope for spatial resolution of a few micrometers, possibly even smaller than the infrared FEL wavelength. This will allow to perform mappings of the absorption profile at the surface of the sample, i. e. microspectrometry. It seems even possible to reach a sub-wavelength resolution.

The experiment was carried out at the CLIO FEL in Orsay/France. The border range between the O^+-implanted and pure germanium region was investigated by recording time curves of the deflection signal at distinct positions of the substrate surface.

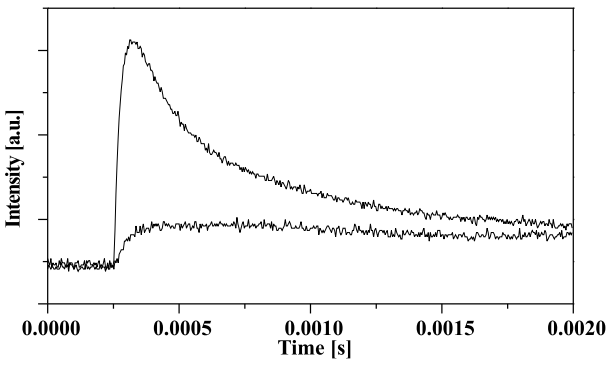

Fig. 1 *Beam deflection signal, measured for different regions of the Ge-substrate at a FEL wavelength of 11.6 μm. Upper trace: O^+-implanted region. Lower trace: untreated region of the substrate.*

For these measurements a constant FEL wavelength of 11.6 μm, which corresponds to the maximum of an absorption line in the generated Ge-oxids was used. Due to absorption the produced germaniumoxide shows an enhanced deflection signal whereas pure germanium is nearly transparent and only a weak deflection signal is observed (Fig.1).

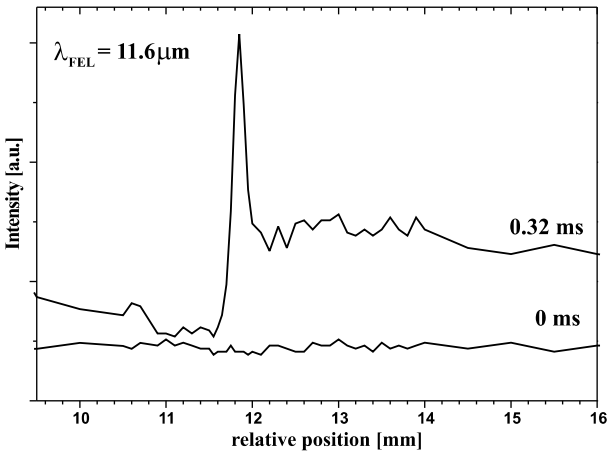

Fig. 2 *Intensity of the deflection signal at distinct positions of the Ge-substrate at 0.32 ms and 0 ms after the FEL pulse, respectively.*

From these time curves profiles representing the absorption at each position of the sample can be obtained reflecting the distribution of the implanted oxygen in the substrate. Figure 2 shows the profiles obtained 0.32 ms after the FEL pulse where maximum deflection was observed. For comparison, the profile at 0 ms where no deflection occurs is also shown. In the border range the step width between two acquisition points was 50 μm and was increased to 100 and 500 μm, respectively, in the outer regions of the substrate. This results in a slightly increased noise of the profiles between 11 and 14 mm relative position. The two different regions of the substrate can be clearly distinguished by different levels of absorption around 10 and 17 mm relative sample position, respectively. Surprisingly, in the border range around 11.8 mm relative position the concentration of the produced oxide seems to be considerably increased. If this is due to the implantation process, to surface effects or to artifacts of the spectroscopic technique applied has still to be verified. In further studies our aim is to increase the spatial resolution to a few microns which will be achieved by a better focusing of the probe beam and a more sophisticated sample translation.

[1] O. Benchikh et. al., J. Phys. 727 (1985) 727

[2] W. Seidel et al., FZ Rossendorf, Wiss. Tech.-Ber. FZR-319 (2001) 36

[1] *FZR, Institute of Radiochemistry,* [2] *LURE, Université de Paris-Sud, Orsay, France*

Temperature Stabilization of the Out-Coupling Mirror Wheel

W. Seidel, M. Sobiella, D. Wohlfarth, U. Wolf, B. Rimarzig

For the U27 Free-Electron Laser (FEL) the so-called hole coupling method, using broad-band metal mirrors with an on-axis hole in one of the mirrors was selected. To optimize the extraction ratio in the whole wavelength range we use 5 mirrors with different holes [1].
The Au coated Cu-mirrors are mounted on a revolvable holder (wheel). To bring one of the mirrors in the right position for lasing, we use a high-precision rotating stage. Despite the small absorption of about 1 % in the mirror, the entire construction will be heated up to a higher temperature during the normal laser operation. This will lead to a change in the resonator adjustment (length and angle) by thermal expansion and to an unacceptable heat load of the precession mechanics.
We estimate a permanent heating power of about 10 W at the mirror for an intracavity power of up to about 1 kW. Heating the mirror in vacuum with this power, we measured a saturation temperature of the wheel of around 100^o C after 20 hours. In this case the heat exchange was realized mainly by thermal radiation in vacuum. This temperature is to high for the mechanical layout of the high-precision rotation stage of the construction. At a movable precession construction in ultra-high vacuum a temperature-stabilized system based on water cooling is difficult to be realized. Therefore, we introduced a special heat isolation between the high-precision rotation stage and the wheel. The wheel is also made from Cu to reduce mechanical tension between the mirrors and the surrounding material. Furthermore, the heat exchange is improved by a more flexible heat dissipation to the outside of the vacuum chamber (peltier element or air cooling) rather than by thermal radiation only. To stabilize the mirror wheel temperature we installed a heater in the center of the wheel. In this way, all the components are at the same equilibrium temperature independently of whether the laser is working or not.
Fig. 1 shows the measured temperature in dependence on time applying a permanent heating power of 15 Watt (instead of 10 W for safety reasons). The temperature sensor for the wheel was located at the opposite side of the heated mirror. After 22 hours the saturation temperature of about 50^o C was achieved using the peltier cooler outside. We observed a temperature difference between mirror and wheel of about 4^o C, which originates from the temperature gradient inside the wheel. Using air cooling we get a temperature of about 54^o C at the mirror. The stabilization of the mirror temperature around 57^o C, i.e. slightly above laser saturation temperature of 54^o C, is demonstrated in fig. 2. By switching the laser (external heating at one mirror with 15 W) on ($\triangle$) and off (∇), we simulated a working regime of the FEL. The $\bullet$ indicates that moment when the heating system for the wheel is switched on. The maximum temperature difference of 3.5^o C over 20 minutes in the mirror leads to a change in the cavity length of about 1 μm. This effect has a small influence on the FEL operation.

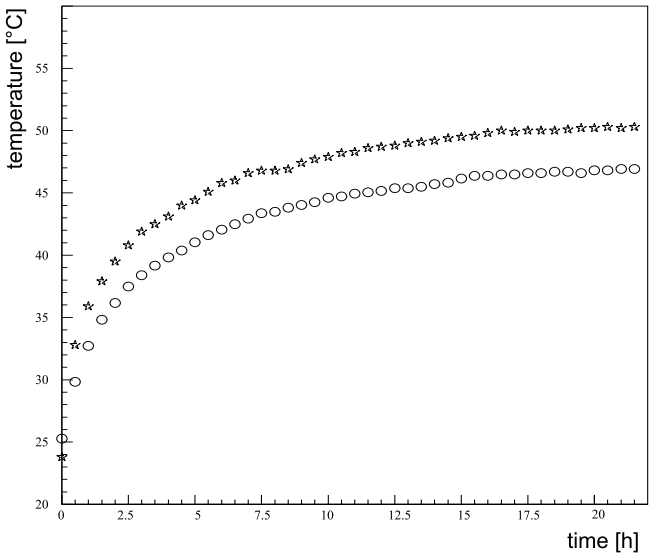

Fig. 1 *Temperature dependence of the working mirror ($\star$) and the wheel ($\circ$) with permanent heating (15 Watt) and cooling using a peltier element (see text).*

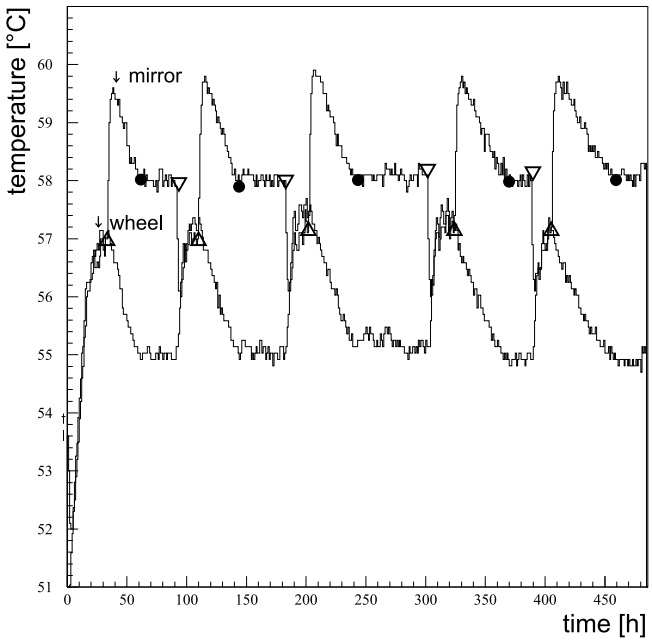

Fig. 2 *Temperature behaviour of the mirror and the wheel during a simulation of a working regime of a FEL (see text; $\triangle$ laser switched on, ∇ laser switched off, $\bullet$ heating of the mirror wheel switched on).*

[1] W. Seidel, E. Grosse, D. Oepts, B. Rimarzig, U. Wolf, FZ Rossendorf, Wiss.-Tech. Ber. FZR-341 (2002) 26

A Four Pole Magnetic Chicane for Phase Matching

P. Gippner

The undulator U27 consists of two separate sub-systems with a drift space d (free of field) between them. By variation of the gap width g the optical wave length is changed and consequently the phasing between the undulator sections has to be changed as well. This is usually done by properly choosing the electron flight path between the sections by varying the drift space d or by a chicane increasing the electron beam path length with respect to a copropagating light ray. Such a chicane may consist of three [1-3] or four dipoles [4] deflecting the electrons only to one side or to both, the left and the right hand side, respectively. The design of a suitable chicane consisting of 4 dipols is shown in fig. 1. The corresponding calculations have been done using the code RADIA[5].

The fig. 2(a) indicates three typical field distributions within a chicane adjusted along the z-axis. The outer and the inner magnets exhibit the same absolute field values $|B_0|$ since the coils of the dipols (D1, D4) and (D2, D3) operate in series and will be supplied by the currents I_1 and I_2, respectively. The trajectories of electrons with a kinetic energy of E = 20 MeV for three different field strenghts are shown in fig. 2(c). For dedicated current values the electrons cross the z-axis at the same intersection point, what can be used for Compton scattering of infrared light quanta stored within the resonator. Fig. 2(b) indicates the angle of the electron velocity vector with respect to the z-axis. The value of this angle can easily be changed by the currents. The table contains the calculated parameters of the electron path within the chicane at E = 20 MeV.

It is the main purpose of future investigations to confirm experimentally the calculated current ratios I_1/I_2 for which the chicane should deliver a correct phasing.

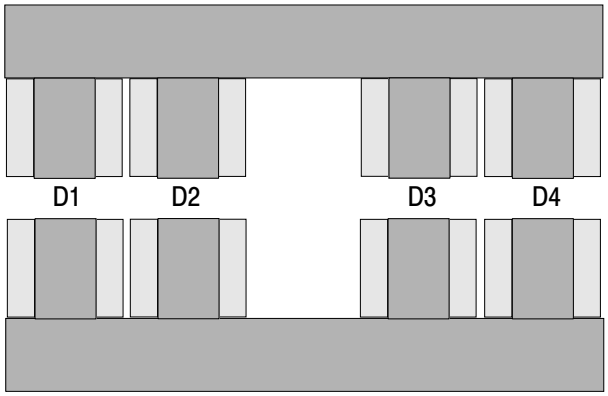

Fig. 1 *Cross section of the projected four pole chicane. The dipoles D1 ... D4 have the same dimensions. The wide interval between the dipoles D2 and D3 forms a space for a flange of the vacuum chamber.*

I_1xn	I_2xn	$\frac{\alpha}{rad}$	$\frac{x_s}{mm}$	$\frac{L}{mm}$	$\frac{\tau}{10^{-9}s}$
-600	+963	0.035	0.0056	320.057	1.0679
-800	+1338	0.049	0.0003	320.108	1.0681
-1000	+1720	0.062	0.0029	320.177	1.0683

Table 1 *Parameters of the electron path (E=20 MeV) within the chicane; α, x_s: angle and displacement at the intertsection point z=0 mm; L, τ: path length and time of flight within the z-interval [-160, +160].*

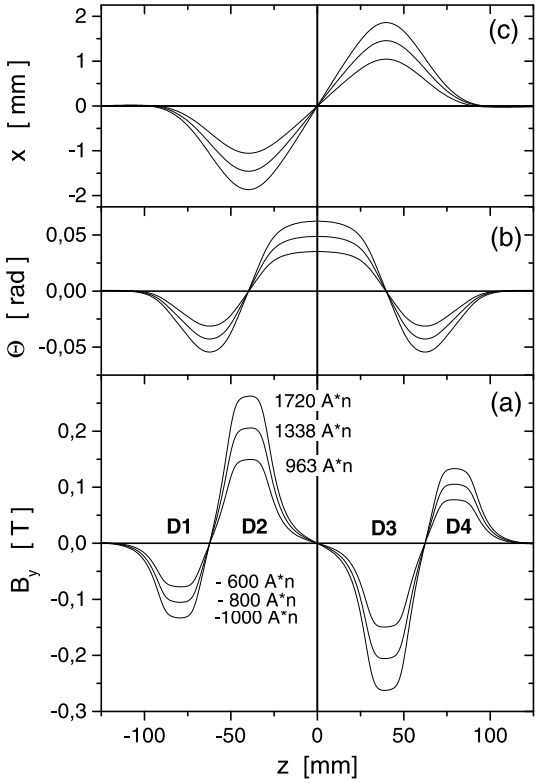

Fig. 2 *Field distributions within the four pole chicane (a) for three dedicated values Ampere* turns and the corresponding trajectories for an electron with the kinetic energy of E = 20 MeV(c). The symbol θ indicates the angle of the electron velocity vector relative to the z-axis (b).*

[1] J. Pflüger, M. Tischer, TESLA FEL 2000-08, December 2000
[2] R. Wünsch et al., Contributions to the 23rd International free Electron Laser Conference, II-61, Darmstadt, Germany, August 20-24, 2001
[3] P. Gippner, FZ Rossendorf, Wiss.-Tech. Ber. FZR-341 (2002) 28
[4] S. Benson, G. Biallas, T. Hiatt, J. Karn, Jefferson Nat. Acc. Facility
[5] P. Elleaume, O. Chubar, J. Chavanne, Journ. Syn. Rad. 5 (1998) 481

New Elements of the GPT Code to Simulate a Resonator Free-Electron Laser

R. Wünsch, C. A. J. van der Geer[1], S. B. van der Geer[1], M. J. de Loos[1]

New elements of the computer code GPT [1] are being developed to simulate the energy transfer in a free-electron laser. In contrast to the single-frequency simulations applied so far the new elements allow us to study the spectral evolution of short laser pulses in a sufficiently large frequency range around the resonance frequency. For that reason we expand the electromagnetic field in a series of resonator eigenmodes with the frequency spacing $\Delta\nu = c/2L_R$ with the resonator length L_R. For the 11.53 m long ELBE resonator the spacing is $\Delta\nu = 13$ MHz. To study the evolution of a laser pulse one has to consider an interval in the order of 1 THz, i. e. roughly 80 000 eigenmodes.

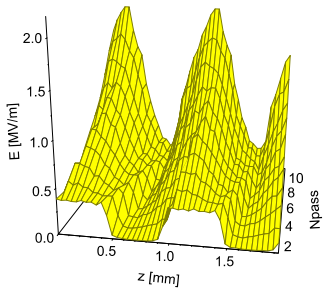

Fig. 1 *Amplification of a wavetrain during 20 passes in a* FEL. *The radiation is modeled with 20 (N = 21922) modes. The corresponding pulse repetition frequency is obviously too high. The radiation pulses overlap.*

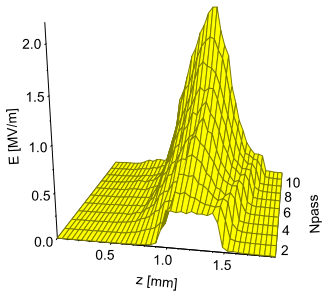

Fig. 2 *The same as in Fig. 1 but modeled with 200 (N = 2296) modes, a ten times lower* PRF. *The pulses do not overlap.*

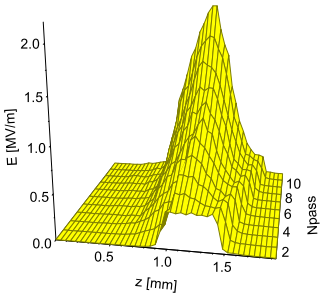

Fig. 3 *As Fig. 1 but with 2000 (N = 230) modes. The result is the same*

To reduce the number of modes to a manageable level we increase the frequency spacing by a factor N with the consequence that a single optical pulse in the resonator is replaced by a series of N pulses separated by a distance $D = 2L_R/N$ from each other. If D is much larger than the length of the pulses they do not overlap and we can consider any member of that pulse train as a representative of the actual pulse. Considering their interaction one has to take into account that a short electron pulse interacts with only one member of the optical pulse train.

The pulses produced by an IR FEL, driven by a RF accelerator, are not longer than a few millimeters. In this case, N can be chosen as large as 10000 with the reduction in CPU time by the same factor without overlapping of the various pulses. Figs. 1-3 show the evolution of a pulse, roughly 1 ps long, within different bases of frequency spacing.

The introduction of macro-particles, which are necessary to manage the large number of electrons in the pulse, distorts the ratio between induced and spontaneous emission in favor of the latter. To get a realistic picture of the induced emission one has to reduce artificially the contribution of the spontaneous process. One way to do that is the introduction of copropagating positively charged macro-particles annihilating the spontaneous emission [2], or by copropagating identical bunches at the opposite side of the ponderomotive wave [3]. We have combined both methods to suppress the exaggerated spontaneous emission almost completely. To describe the start-up from noise where the spontaneous process is essential we introduce a seed electron without copropagating positive charge.

Fig. 4 shows the calculated gain of optical power for a very low initial field strength for our electron bunch modeled with 100 macro-particles accompanied by the corresponding positive charge and copropagating bunches. The data reproduce the expected behavior of induced emission without any visible contribution from spontaneous emission.

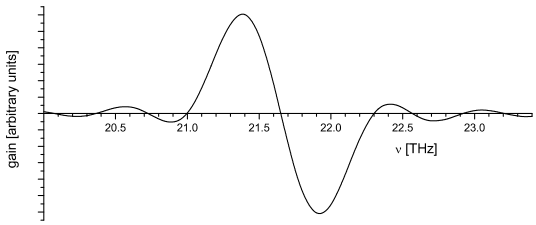

Fig. 4 *Single-pass gain versus frequency ν calculated for 0.1 V/m initial field strength and 100 macro-particles representing a monoenergetic electron bunch with a charge of $Q = 50$ pC and 20 MeV kinetic energy.*

The power of the optical pulse in the equilibrium after a few hundreds of passes through the resonator is an important quantity to be predicted. To accelerate the power build-up we use a seed particle as described above. In this way the calculation time is remarkably reduced.

[1] M. J. de Loos, C. A. J. van der Geer, S. B. van der Geer, 3D Multi-Frequency FEL Simulations with the General Particle Tracer Code, EPAC 2002, Paris, France, pp. 849; S. B. van der Geer, M. J. de Loos, The General Particle Tracer Code, Thesis TU Eindhoven 2002, ISBN 90-386-1739-9; Pulsar Physics, General Particle Tracer, http://*www.pulsar.nl*

[2] V. Litvinenko, O. Shevchenko, Proc. of the 24th Int. Free Electron Laser Conference 2002, Argonne, USA

[3] M.J. de Loos, C.A.J. van der Geer, S.B. van der Geer, A.F.G. van der Meer, D. Oepts, R. Wünsch, Proc. of the 24th Int. Free Electron Laser Conference 2002, Argonne, USA

[1] *Pulsar Physics, The Netherlands*

Start-Up Simulations of the Spectral and Spatial Evolution of the ELBE FEL

R. Wünsch, C. A. J. van der Geer[1], S. B. van der Geer[1], M. J. de Loos[1]

We have used the new elements [1] of the GPT code [2] to simulate the temporal evolution of the optical beam in the ELBE FELs. The parameters of undulator and electron beam used in the calculation are displayed in table 1.

Undulator	
Number of periods	34
Period length	27.3 mm
Undulator parameter $K_{\rm rms}$	1
Electron beam	
Energy	20 MeV
Energy spread	72 keV
Pulse charge	50 pC*
Pulse length	0.7 ps (210 μm)
Optical beam	
Resonance frequency	21.56 THz
Frequency range	19.8 .. 22.9 THz
Number of long. modes	200
Round trip loss	5%
Resonator length	11.53 m
Rayleigh range	1 m

Table 1 *Parameters of undulator, electron and optical beam as used in the calculations.*
** The 77 pC pulse charge of ELBE has been reduced to 50 pC. This is to simulate the gain degradation caused by the roughness of the undulator field.*

Fig. 1 shows the evolution of the total laser power without resonator detuning, i. e. the round-trip time of the light corresponds exactly to the repetition rate of the electron bunches. The effect of a finite resonator detuning will be investigated in a separate paper [3]. The calculations have been performed with 200 longitudinal modes equidistantly distributed between 19.8 and 22.9 THz. The build-up time has artificially been reduced by means of a seed particle with the charge $Q = -1$ pC.

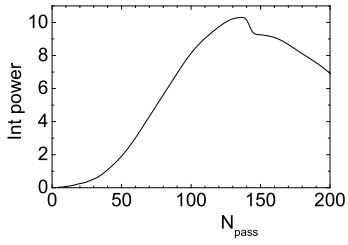

Fig. 1 *Evolution of the total intracavity radiation power (in arbitrary units) as a function of the number of passes $N_{\rm pass}$.*

Figs. 2 and 3 display the spectral and spatial evolution of the first 200 passes.

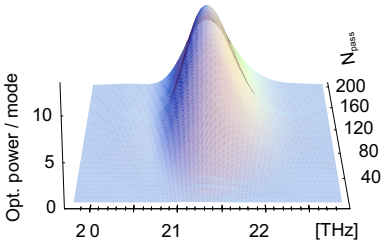

Fig. 2 *Internal laser power per mode as a function of frequency ν and number of passes $N_{\rm pass}$*

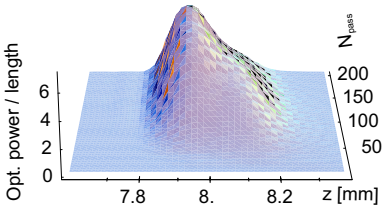

Fig. 3 *Internal laser power as a function of the longitudinal coordinate z and the number of passes $N_{\rm pass}$*

The optical pulses evolve in quite a smooth manner, both in frequency and real space. When the power increases, the spatial distribution narrows and the peak shifts towards the rear end of the pulse. This part of the optical pulse has been amplified at the rear part of the undulator where the gain is larger than in the front part due to the onset of microbunching. Consequently, the centroid of the light pulse is traveling slower than light in vacuum (c). The light pulse drifts away from the electron pulse, the gain reduces and falls below the loss in the resonator and the optical power begins to decay.

The effect described above is denoted as laser lethargy. It occurs when the electron pulses are shorter than the slippage length $\Delta = N_{\rm u}\lambda$. We have used $\mu_{\rm c} = \Delta/\sigma_z \approx 2.3 > 1$ in the calculation.

Laser lethargy can be compensated by reducing the resonator length $L_{\rm R}$ from the value synchronized with the repetition rate of the electron bunches, so that the smaller group velocity of the light pulse is compensated.

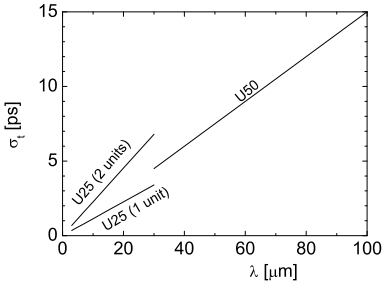

Fig. 4 *Electron pulse lengths σ_t corresponding to the condition $\mu_{\rm c} = 1$ as a function of the laser wavelength calculated for the undulators of ELBE.*

Fig. 4 displays the rms electron pulse lengths satisfying the condition $\mu_{\rm c} = 1$ (pulse length equals slippage length). Pulses around this value or shorter are expected to be affected by the lethargy problem.

[1] R. Wünsch,C. A. J. van der Geer, S. B. van der Geer, M. J. de Loos, This Report, p. 57
[2] M. J. de Loos, C. A. J. van der Geer, S. B. van der Geer,
3D Multi-Frequency FEL Simulations with the General Particle Tracer Code, EPAC 2002, Paris, France, pp. 849;
S. B. van der Geer, M. J. de Loos, The General Particle Tracer Code, Thesis TU Eindhoven 2002, ISBN 90-386-1739-9;
Pulsar Physics, General Particle Tracer, http://*www.pulsar.nl*
[3] R. Wünsch,C. A. J. van der Geer, S. B. van der Geer, M. J. de Loos, This Report, p. 61

[1] *Pulsar Physics, The Netherlands*

Simulation of Limit Cycle Oscillations in the U27 FEL

R. Wünsch, C. A. J. van der Geer[1], S. B. van der Geer[1], M. J. de Loos[1]

Limit cycle oscillations in a short-pulse FEL, as a result of a periodic, self-replicating micropulse structure on successive cavity transits, were first predicted by Colson [1]. First experimental evidence was given in ref. [2]. To understand this phenomenon one has to remember the following features of the interaction in a FEL. Electrons slip back relative to an optical micropulse on their mutual travel through the undulator, due to the difference in forward velocity. As a consequence, the optical micropulse is stronger amplified at its trailing edge. In other words, its group velocity is somewhat smaller than the vacuum value. A micropulse stored in a perfectly synchronized resonator grows, narrows and retards on successive passes through the undulator, with the consequence that the laser gain is reduced (laser lethargy). In order to restore the gain, it is necessary to slightly desynchronize the resonator, which usually is done by reducing the cavity length. When the laser intensity approaches saturation the gain at the highest intensity is reduced first. As a result the center of power is shifted forward and the group velocity becomes larger than the value of optimum overlap between optical and electron pulse. The gain starts to decrease and the power falls below the saturation level. From now on another oscillation starts whereby the center of optical power performs an oscillation in the well of the ponderomotive potential. Limit cycle oscillations do only occur when the electron pulse is shorter than the slippage length $N_u\lambda$ (N_u: number of undulator periods, λ: radiation wavelength). Otherwise the oscillations are washed out.

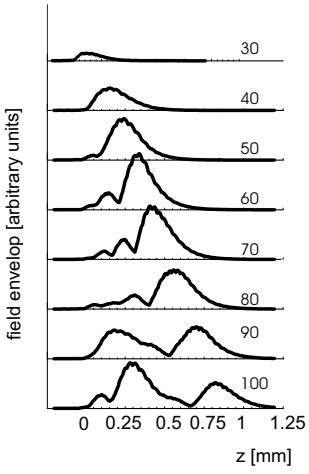

Fig. 1 *Envelope of the radiation field at the undulator exit after 30, 40, . . . , 100 passes calculated for one unit of the U27 undulator of ELBE (parameters see table 1 of ref. [4]). The resonator detuning is -0.5λ and 5% round-trip loss has been assumed.*

We have simulated such kind of oscillations for the ELBE FEL by means of the code GPT [3]. Fig. 1 shows the evolution of the envelope of the optical pulse. First, the optical pulse grows with the peak near to the trailing edge. Since the resonator is shorter than the value corresponding to the electron repetition rate the optical pulse moves forward from pass to pass. After 50 passes a second peak starts to grow at the trailing edge where the overlap with the electron pulse is large. This peak grows fast since the electron pulse has been prebunched by the strong field in the first part of the undulator. The leading edge of the pulse looses the overlap with the electron pulse and decays in dependence on the resonator loss. As a result, the center of the optical peak moves forth and back in the ponderomotive well. This oscillation produces side lobes in the spectrum which emerge and vanish periodically (see Fig. 2).

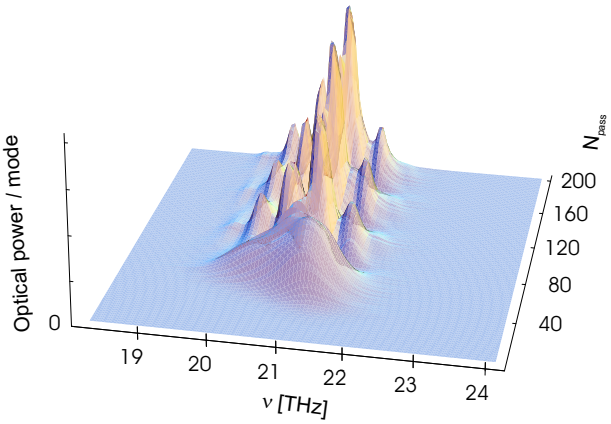

Fig. 2 *Evolution of the total radiation power as a function of frequency ν and number of passes N_{pass} calculated for the same parameters as in Fig. 1.*

Frequency and amplitude of the observed limit cycle oscillations depend on resonator detuning and round-trip loss. In Fig. 3, we vary the detuning from a value much smaller to a value much larger than the value giving optimum gain. At lower detuning the laser starts slowly but saturates at a higher power level which is characterized by remarkable oscillations. Detuning the resonator stronger than the value of optimum gain leads to both a small gain and a lower power level at saturation.

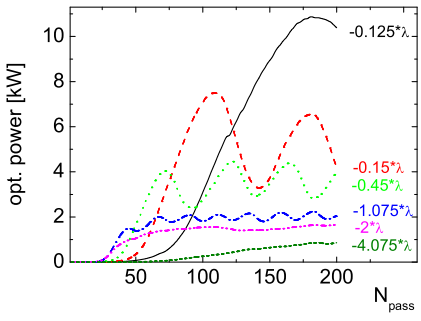

Fig. 3 *Evolution of the total laser power as a function of the number of passes N_{pass} calculated for the same parameters as in Fig. 1 and the indicated values of the resonator detuning.*

[1] W. B. Colson, Phys. Quantum Electron. 8 (1982) 457
[2] D. A. Jaroszinski, R. J. Bakker, A. F. G. van der Meer, D. Oepts, P. W. Amersfoort, Phys. Rev. Lett. 70 (1993) 3412-3415
[3] R. Wünsch,C. A. J. van der Geer, S. B. van der Geer, M. J. de Loos, This Report, p. 59
[4] R. Wünsch,C. A. J. van der Geer, S. B. van der Geer, M. J. de Loos, This Report, p. 60

[1] *Pulsar Physics, The Netherlands*

Dynamics of Matrix–Isolated Molecules [E]

J.A. Piest

Gaining insight in intra- and intermolecular processes is an important issue in order to understand physical, chemical, and biological reactions in micro- and macroscopic systems. Such reactions determine the way molecules interact with their environment. For example, formation of amino-acids takes place in interstellar ice analogues [4, 5], which can be studied in more detail by time-resolved IR experiments [3].

Detection of time-resolved optical parameters of molecules reveals the time scales of energy redistribution, which governs such processes. Therefore, it can be used as a powerful method to study the dynamics of molecular systems.

The advantage of doing experiments in the region slightly above zero Kelvin is clear: in this condition molecules have much lower internal energies than at room temperature. Generally, in the spectra of such cold molecules there are 1) less transitions present, and 2) the band width per transition is smaller. Thus, spectra of these molecules are less complicated than those recorded for warm species and can be interpreted with less ambiguity.

In particular, time-resolved spectral data of cold molecules may lead to knowledge of the time scales on which intra- and intermolecular energy redistribution takes place, and inform us about the time response of physical or chemical inter(re)actions in molecular systems. Due to lack of bright IR short-pulse light sources, time-resolved spectral data in the sub-nanosecond domain for matrix-isolated species are scarce, where spectra in the available μs region do not yield relevant information [1, 2, 3].

In a user lab of the ELBE building a high vacuum setup is under construction in order to do such experiments with cold molecules. In this setup, isolated molecules are embedded in a molecular or inert gas ice. By mixing of gases more exotic ices, such as interstellar ice analogues, can be generated easily.

The setup consists of two chambers pumped by two Varian V301 Navigator turbo-molecular pumps. Two Varian SH100 membrane pumps provide a sufficiently low roughing pressure.

A liquid helium-cooled Janis ST-400 UHV cold head, operating between temperatures of 1.5 K and 300 K, and with a cooling power of 3 W at 5 K, is to be mounted on one of the chambers. *In situ* sample generation takes place on a transparant surface mounted on the tip of this cold head. Purified gases are mixed with sample species to well defined concentrations, before being deposited on the cryogenically cooled window. Also externally prepared samples can be mounted on the tip of the cold head before evacuating the vacuum chambers and cooling the sample.

Experiments to be done with this setup in order to yield time-resolved spectral information vary from simple one-color pump-probe experiments in direct absorption, to more sophisticated background-free detection methods such as: detection of the photon echo, scattering of IR or UV light on a transient grating, or laser induced fluorescence (LIF). The two latter experiments desire a resonant IR-UV excitation scheme.

In all of these proposed experiments, the absorption of IR light is governed mainly by two laws:

$$\frac{n(\tau,\delta z)}{n(0,\delta z)} = \exp\left(-\frac{\overline{\sigma}}{h\nu}\int_0^{\tau} I(t,\delta z)dt\right), \qquad (1)$$

and:

$$\frac{I(t,\delta z)}{I(t,0)} = \exp\left(-\overline{\sigma}\int_0^{\delta z} n(t,z)dz\right), \qquad (2)$$

the first of which describes the change in the local absorber density $n(t,z)$ in a two level approximation as a function of the time-averaged pulse intensity $I(t,z)$. The second expression is known as the Beer-Lambert law, describing the decay of averaged pulse intensity along a path $(0,\delta x)$ through the sample as a function of the averaged absorber density. The central wavenumber of the IR spectral profile is represented by ν, while the line-integrated absorption cross section is symbolized with $\overline{\sigma}$. Linear absorption is assumed in both expressions, though, similar laws can be derived for non-linear absorption processes.

For the experiments in direct absorption the variation of IR absorption of the probe pulse as a function of time-delay is the relevant parameter to be determined. Depending on the line-integrated cross section of the sample molecule, this variation is usually not larger than a few percent of the total absorption strength. Considering the spectral width of the transition smaller than the IR spectral profile the change in the signal detected may be only a fraction of a percent. Therefore, it is highly desirable to resolve the IR pulse spectrally, for instance by coupling it into a fourier transform infrared spectrometer (FTIR) after passing the sample. The IR pulse, with elongated duration either due to the absorption lines present under the IR spectral profile, or due to an artificial modulation, can then be analyzed. Because natural pulse elongation due to presence of small absorption features may not lead to the desired intensities of the signal to be deteced, simulations to modulate the IR pulse artificially, in order to reveal (partial) information about small structures of the spectral distribution are currently carried out.

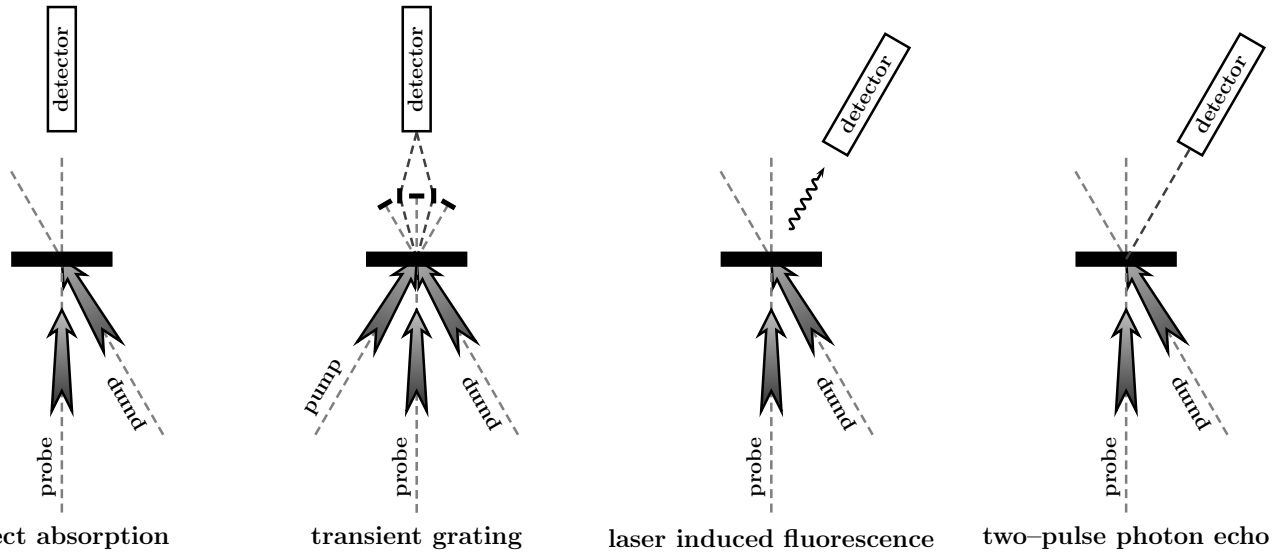

Fig. 1 Experimental setup schemes for time-resolved spectroscopy of matrix-isolated molecules. The sample is represented with a thick black line. Pump and time-delayed probe laser pulses irradiate the sample. (ll) In direct absorption the change in intensity of the probe pulse is recorded as function of the time-delay. (l) Photon yield scattered from a transient grating, generated with two mutually interfering pump pulses, as function of the time-delay yields information about the population of excited molecules in the grating. (r) In an IR-UV double-resonance scheme fluorescence from an excited electronic state is recorded as a function of time-delay between IR pump and UV probe pulse. (rr) Coherent fluorescence is detected as a function of the time-delay between pump and probe pulse.

In case of transient grating scattering and LIF a tunable laser in the UV is desirable. When a resonant IR-UV excitation scheme is applied, the fluorescence or the scattering of UV light on a IR-IR induced grating can be detected against zero background, in fluorescent or non-fluorescent species, respectively. The transient grating scattering method may also yield detectable signal without application of a UV laser, by scattering of IR light on an IR induced grating. Simulations are currently carried out, in order to estimate the yield of scattered photons.

The IR light has to be provided by either the FEL or the Topas, whith a strong preference for the FEL, because of its higher averaged output power as a result of a much higher repetition rate. Scattering of IR light on an IR induced grating may possibly only work with the FEL, due to the feeble signals expected, *i.e.,* some mW of scattered signal with some Watt of resonant input photons.

Applying the two pulse photon echo method the coherent fluorescence (the "photon echo"), yielding information particularly about homogeneous relaxation processes, is detected. The setup for this experiment is apparently similar to the direct absorption pump-probe setup, though, the experiment is more subtle because special care has to be taken for the pump and probe pulse intensities, and for the position of the detector. The direction of the detected signal is determined by momentum conservation: $\mathbf{k}_{photon-echo} = 2\mathbf{k}_{probe} - \mathbf{k}_{pump}$, implying an intensity ratio between the pump and probe beam of 1:2.

The schemes for each of these experiments are depicted in Fig. 1.

In future, besides the matrix-isolation experiments, the setup can be extended easily to do experiments on molecules or ions applying either effasive or supersonic, pulsed or continuous, jets, while exploiting high sensitive ion detection methods.

[1] Allamandola and Nibler, Chemical Physics Letters 28 (1974) 335-340
[2] Allamandola et al., Journal of Chemical Physics 67 (1977) 99-109
[3] L.J. Allamandola, NASA/Ames Research Center, private communications, 2002
[4] Bernstein et al., Nature 416 (2002) 401
[5] Muñoz Caro et al., Nature 416 (2002) 403

Clonogenic Survival of Mammary Epithelial Cells MCF-12A after Irradiation with 200 kV X-Rays

A. Panteleeva, W. Dörr[1], E. Lessmann, J. Pawelke

Precise determination of the relative biological effectiveness (RBE) of low-energy X-rays ($E_{ph} \leq 50$ keV) is important because of their widespread use in diagnostic radiology and radiotherapy. However, literature data on this topic is still not conclusive. Recently, RBE of 25 kV X-rays was determined for the survival and chromosomal damage by micronucleus test for 4 human and rodent cell lines [2]. Since X-rays of this energy range are used especially in mammography, the study was extended to human mammary epithelial cells. Most human cancers are of epithelial origin, therefore, they represent an appropriate model system for testing the cell kill and induction of genetic damage. The established cell line MCF-12A was cultured in the cell laboratory at ELBE (Fig. 1) and cell culture parameters were optimized. The cell line, purchased from ATCC (USA), is a non-tumorigenic epithelial cell line established from tissue taken at reduction mammoplasty. The line was produced by long term culture in serum free medium with low calcium concentration. MCF-12A was derived from adherent cells in the population, by a transformation resulting from a 72 h exposure to 45^0C [2]. The cells were incubated at 37^0C in humidified athmosphere containing 5% CO_2, in a one to one mixture of DMEM and Ham's F12 supplemented with 5 % horse serum, 500 ng/ml hydrocortisone, 0.01 mg/ml insulin, 100 ng/ml cholera toxin and 20 ng/ml epidermal growth factor.

The cell line was proved to be suitable for long-term culture, necessary for the future experiments on RBE determination by cell survival and micronucleus test. The plating efficiency was determined to be 51.8 ± 0.9 %, independent on the passage number (Fig. 2). The cells were irradiated at the Radiotherapy Department of the Medical Faculty of the TU Dresden. The X-ray tube (tungsten anode, 0.5 mm Cu filtration) was operated at 200 kV and 20 mA. The cells were seeded in 25 cm^2 polystyrene flasks and irradiated as monolayers in the exponential growth phase, before reaching 70 % confluence. The dose rate was 1.2 Gy/min, and doses of 1 to 10 Gy were applied. Immediately after irradiation, cells were trypsinized and seeded at low density in Petri dishes at 10 replications per dose point. After 11 days incubation, the colonies were fixed and stained. Colonies with more than 50 cells were scored as survivors. The data were fitted to the linear-quadratic model $S = exp(-\alpha D - \beta D^2)$. The survival data as well as the fitting parameters α and β are presented in Fig. 3. The surviving fraction at 2 Gy (SF2) was calculated to be 0.43 ± 0.03. Data were also fitted to the single hit - multitarget model $S = 1 - (1 - exp(-D/D_0))^n$, revealing the parameters $D_0 = 1.43 \pm 0.06$ and $n = 2.2 \pm 0.1$, showing very good agreement with survival data of normal primary mammary cells [3]. As a next step, the determination of survival and chromosomal damage by 25 kV X-ray tube irradiation will be performed.

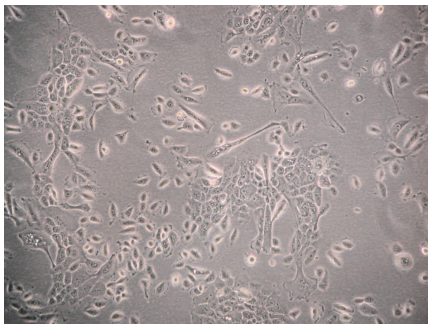

Fig. 1 *Culture of MCF-12A with characteristical epithelial-shaped cells.*

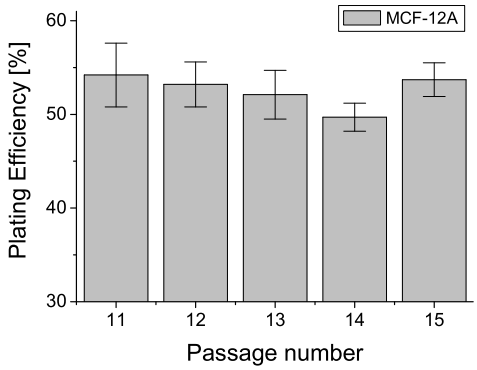

Fig. 2 *Dependence of the plating efficiency on the passage number. The mean values from several experiments are shown together with the standard error of the mean.*

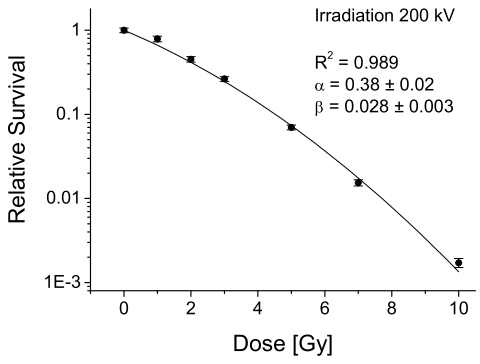

Fig. 3 *Survival of MCF-12A after irradiation with 200 kV X-rays. The values are representing the mean from 8 experiments and the standard error of the mean.*

[1] A. Panteleeva et. al., FZ Rossendorf, Wiss.-Tech. Ber. FZR-341 (2002) 90
[2] T.M. Paine et. al., Int. J. Cancer 50 (1992) 463
[3] L.E. Cathers and M.N. Gould, Int. J. Radiat. Biol. Relat. Stud. Phys. Chem. Med. 44 (1983) 1

[1] *Dept. of Radiotherapy, Medical Faculty, Technical University of Dresden*

Influence of the Handling Procedure During Irradiation on Cell Survival and Micronucleus Test Results

A. Panteleeva, E. Lessmann

The first radiobiological experiment planned to be performed at the ELBE X-ray beam is the determination of RBE of soft X-rays. Obtaining of dose-response curves for at least 5 dose points is required for the exact determination of the curve parameters. Cell survival and chromosomal damage by micronucleus test as biological endpoints will be studied. The required irradiation times at the expected dose rate of $\sim$1 Gy/min and required dose range of 1 - 10 Gy are estimated to be in the order of 0.5 - 1 hour. Taking into account the time-consuming closing and opening the radation protection doors of the radiation physics cave, a total time of several hours has to be expected for the complete handling procedure of cell irradiation. Since the cells have to be outside the optimal environment (37^0C, humidified atmosphere containing 5% CO_2) during this time, additional stress reactions, resulting in increased cell kill or chromosomal damage, have to be expected. On the other hand, determination of damage by micronucleus test requires blocking of the cell cycle. Since the time scale of repair of potential lethal damage is for mammalian cells in the order of up to $\sim$3 hours, it could interfere with the primary damage and result in a reduction of the irradiation effect.

To prove this possibility, experiments on determination of the effect of cell handling in non-optimal conditions were performed. For the cell survival assay, the cells were seeded in the cell culture dishes, filled with medium and sealed. The cell culture dishes PetriPerm with a 25 μm membrane base (Sartorius, Göttingen) have been chosen for cell irradiation at the ELBE X-ray beam [2]. Since the X-ray beam at ELBE is horizontal, the cell dishes were kept in a vertical position during this simulation procedure for 0, 2, 4, 6 or 8 hours. A cell culture flask was used for additional control. Afterwards, the cells were trypsinized and the standard clonogenic assay was performed. The results shown in Fig. 1 for the cell line MCF-12A and in Fig. 2 for NIH/3T3 show no significant change in plating efficiency due to the handling in non-optimal conditions.

The influence of the handling procedure on the micronuclei outcome was also studied for these cell lines. The cells were irradiated with UVC light (253.7 nm) and then left for 0, 0.5, 2, 4 or 6 hours at 20^0C or at 0^0C (ice). Afterwards, the standard micronucleus test was performed. The results in Table 1 show that the time interval of up to $\sim$2 h is not influencing the test result (keeping the cells on ice or at room temperature), however, the spread of the fraction of binucleated cells after 6 h handling shows the influence of the inoptimal conditions. Therefore, for this test it is desirable to keep the handling times less than 2 hours.

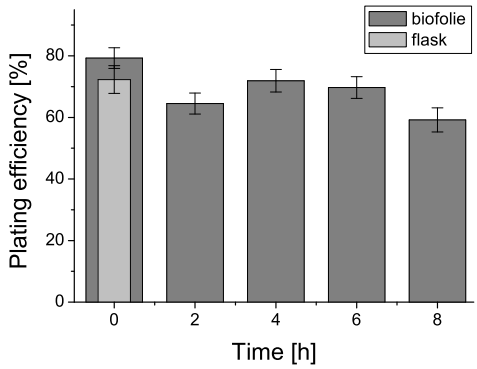

Fig. 1 *Dependence of the plating efficiency for MCF-12A on the handling time. The mean value of 1 experiment (10 replications) together with the standard error of the mean is shown.*

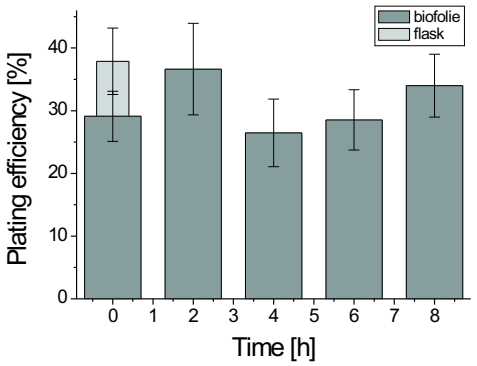

Fig. 2 *Dependence of the plating efficiency for NIH/3T3 on the handling time. The mean value of 1 experiment (10 replications) together with the standard error of the mean is shown.*

Tab. 2 *Fraction of binucleated cells with micronuclei after 0, 0.5, 1, 2, 4, 6 h handling procedure for NIH/3T3 (1 experiment) and MCF-12A (3 experiments).*

Cell line	T [^{0}C]	0 h, no irradiation	0 h	0.5 h	1 h	2 h	4 h	6 h
3T3	20^0C	0.8±0.2	3.4±0.4	4.3±0.3	5.3±1.1	4.8±0.6	-	4.2±0.6
	0^0C			4.2±0.2	4.3±0.2	3.8±0.2	-	2.8±0.2
MCF-12A	20^0C	4.7±0.7	13±2	13±2	16±2	14±2	9.3±1.0	16±2
	0^0C			14±2	16±1	13±2	14±2	19±2

[1] A. Panteleeva et. al., FZ Rossendorf, Wiss.-Tech. Ber. FZR-341 (2002) 89

Measurements of Spectral Dose Distributions of a Soft X-Ray Tube

J. Pawelke, A. Panteleeva, C. Hoinkis[1]

RBE values of X-rays from a conventional 25 kV soft X-ray tube have been determined for cell survival and chromosomal damage (formation of micronuclei) by irradiation of several cell lines [1]. Significantly higher induction of micronuclei was observed after irradiation with 25 kV X-rays in comparison to the reference radiation from a 200 kV X-ray tube. RBE values for the different cell lines were found to be between 1.1 and 1.3. In contrast, the RBE at 10 % survival was found to be not significantly different from 1 for all cell lines. Further experiments at lower X-ray energy are desirable in order to study the X-ray energy dependence of the RBE.

The tungsten anode soft X-ray tube (Darpaq 150-MC) is used for therapy. When operated at 25 kV and 20 mA with 0.3 mm Al filter, the dose rate at the target position was measured by an air filled ionisation chamber (23342, PTW Freiburg) to be 1.67 Gy/min. Since photon energy dependent dose cannot be measured by ionisation chambers (IC), it was calculated after determination of spectral photon flux density by considering the energy dependent energy absorption coefficient for water. The photon flux was measured with a high resolution 13 mm^2 Si-PIN diode (XR100-CR, Amptek, Bedford, USA). The necessary flux reduction was achieved by operating the tube at 0.2 mA current and by mounting a 25 μm iron slit collimator (5 mm thick) in front of the detector. By moving the detector perpendicular to the slit orientation with a step motor unit the maximum photon intensity was determined for dose calculation. Energy distribution was acquired at a count rate of about 1000 photons/s in order to minimise detector pile-up effect. For this purpose, the detector was placed within the X-ray cone at farthest possible distance from the focal spot and moved up to $\approx$3 mm out of center. The detector was calibrated by measuring the spectra of several sources (^{55}Fe, ^{241}Am, ^{210}Pb) as well as of X-ray fluorescence produced in a thin lead foil. The detector energy resolution was measured to be 304 eV FWHM at 5.9 keV.

Removal of the 0.3 mm Al filter results in a more than threefold increase of photon flux density and a decrease of mean X-ray energy (Fig. 1). Reducing the tube high voltage further decreases the mean photon energy and simultaneously the intensity. This intensity loss is compensated by the increase of the mass energy absorption coefficient with decreasing photon energy (see Table 1). Consideration of detector and collimator geometry as well as detector dead time and efficiency correction results in a reasonable agreement between dose rate directly measured by IC with those calculated on the base of photon flux measurement (Table 1). The dose rate calculated in this way is less accurate than the one measured by IC, however, useful in determining the spectral dose distribution (Table 2). Measurements were repeated with a 9 mm^2 cadmium zinc telluride detector (XR-100T-CZT, AmpTek, USA) which confirms all results mentioned above. The next cell irradiations will be performed for tube operation at 10 kV.

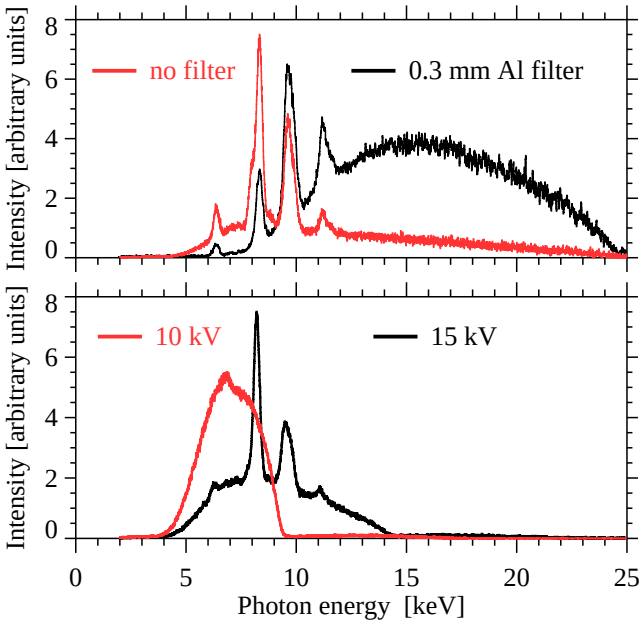

Fig. 1 *Energy distribution of the soft X-ray tube intensity, measured with a low-energy X-ray detector (XR100-CR), corrected for the detection efficiency. The upper part shows the effect of X-ray filtration for tube operation at 25 kV, whereas the influence of the tube high voltage is shown in the lower part (no filtration). The small peak at 6.4 keV arises from the K_α line of iron fluorescence of the collimator.*

Tab. 1 *Photon intensity I_γ and dose rate $\dot{D}$ at the target position for tube operation at 0.2 mA current.*

Tube parameter	I_γ ph/s	$\dot{D}$ $[mGy/min]$ IC	Detector
25 kV, Al filter	12285	2.1±0.2	2.6±0.9
10 kV, no filter	7080	2.6±0.2	3.3±1.0

Tab. 2 *Spectral dose contribution from soft X-ray tube in dependence on tube operation parameters.*

Photon energy [keV]	Dose contribution [%] 10 kV no filter	15 kV no filter	25 kV no filter	25 kV 0.3 mm Al
4... 7	47.6	19.3	12.0	1.4
7...10	50.9	60.7	60.1	23.5
10...13	0.9	17.1	15.8	28.0
13...19	0.6	2.7	10.1	37.2
19...25	0.0	0.2	2.0	9.9

[1] A. Panteleeva et al., FZ Rossendorf, Wiss.-Tech. Ber. FZR-341 (2002) 90

[1] *Dept. of Radiotherapy, Medical Faculty, Technical University of Dresden*

Changing the Dose Range of TSEE Dosimeters

A. Panteleeva, E. Lessmann, J. Pawelke

The TSEE detectors have been studied as a possible solution for dosimetry in a living cell. The small thickness of the sensitive layer ($\sim$ 10 nm) allows to sample the depth-dose distribution even on the scale of cell dimensions (thickness $\sim$ 5 μm), an important feature in the case of soft X-rays. The study of these detectors proved their good reproducibility under laboratory conditions [1]. Another important characteristics is the possibility of simulation of irradiations in real cell environment conditions such as liquid medium. This was proved possible, with stable detector response also in liquid (propanol) [2]. However, the saturation of dose response due to the limited pulse resolution of the gas-flow counter resulted in an upper detection limit of $\sim$ 0.1 Gy, far from the range required for cell survival studies ($\leq$ 10 Gy). This limitation can be overcome by manipulation of the readout system (counter geometry, gas flow), which however results in little increase of upper response limit. Another possibility is to change the irradiated detector area, but it results in difficult detector handling. Therefore, detectors produced by two new methods were tested. The first method is the sedimentation of BeO water suspension on a graphite substrate (detector type II). This method is very simple, results in one TSEE peak (Fig. 1) and allows to vary the amount of the BeO and therefore the detector sensitivity. However, a fading effect was observed, expressed in several orders of magnitude drop of the response to irradiation on the first days after production (Fig. 2). The properties of the detectors, studied after stabilisation of the response, are presented in Table 1. Detectors type III were produced by impregnation of a 1 mm graphite plates with Be and subsequent oxidation at 1400^{0}C by Dr. Holzapfel Messgerätelabor, Teltow. Three detectors produced in this way with low, medium and high sensitivity were studied and compared to detector type I, which shows up to now the best reproducibility [1]. A fading effect for detector type III was not observed (Fig. 2). The irradiation in liquid (propanol) for both detector types II and III resulted in good reproducibility of response, however, the mean response for detector type II was reduced, although the expected attenuation in this layer thickness is negligible (Table 2). Therefore, detectors type II can be used in cases where the simplicity of detector structure is more important than the reproducibility of response and are inappropriate for simulation of the real cell geometry. The method of production of detector type III can be used to vary the dose response, but the reproducibility of response of these detectors has to be still optimised.

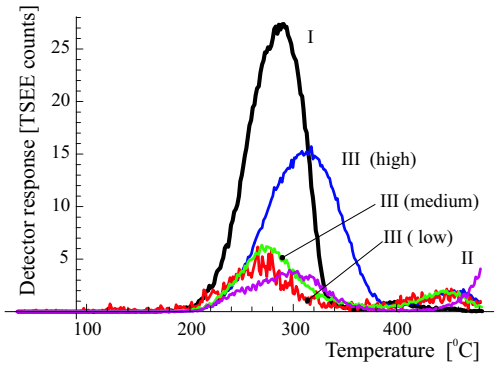

Fig. 1 *Glow curves of the new detector types II and III. For better illustration, the glow curve of detector type III (low) is multiplied by a factor of 100. The response of detector type I is shown for comparison.*

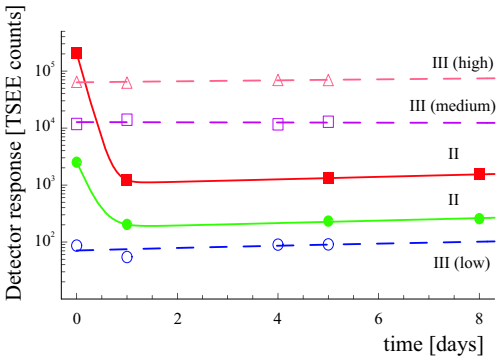

Fig. 2 *Fading effect: the detecor response is evaluated immediately after the irradiation with a ^{90}Sr source in air. This procedure is performed on several consecutive days after the detector production.*

Tab. 1 *Main properties of TSEE detectors.*

Detector type	Sensitivity [counts/mGy]	Reproducibility [a] in air (^{90}Sr) [%]
II	5690	9.2
III (low)	49	8.6
III (medium)	6406	13.2
III (high)	30637	4.7
I	7790	0.82

[a]) Average deviation from the mean of 10 measurements

Tab. 2 *Response of detectors type II and III to irradiation in liquid.*

Detector type	Reproducibility [a] in propanol (^{22}Na) [%]	Spacing [b] [mm]	Response [a] ratio air to propanol (^{22}Na)
II	13.8	2.8±0.2	1.6±0.2
III	15.3	2.0±0.2	1.4±0.3

[a]) Average deviation from the mean of 8 - 10 measurements
[b]) Detector to source distance, filled up with air or liquid

[1] J. Pawelke and A. Panteleeva, FZ Rossendorf, Wiss.-Tech. Ber. FZR-319 (2001) 102
[2] A. Panteleeva et. al., FZ Rossendorf, Wiss.-Tech. Ber. FZR-341 (2002) 92

An X-Ray Monochromator for the Channeling Source at ELBE

J. Pawelke, A. Heitsch[1], A. Panteleeva, M. Sobiella

An X-ray source is being developed at ELBE, where quasi-monochromatic X-rays will be produced by electron channeling in diamond crystals [1]. In order to separate the channeling radiation (CR) from the polychromatic bremsstrahlung background a first X-ray monochromator has been designed for CR of 18.4 keV mean energy. Optimal monochromator properties will be achieved by coating the curved surface of a stepped mould with highly oriented pyrolytic graphite (HOPG) crystals [2]. The mould geometry is shown in Fig. 1 where steps of same curvature are merged and the outer part is extended to result in a rectangular shape for practical reasons (cf. Fig. 2 in [2]).

For the mould a material with the following properties is required: *(i)* radiation resistant, *(ii)* low Z in order to minimise photon scattering, *(iii)* machinability with high precision of the final curvature, *(iv)* adherence of the HOPG crystals to mould surface without glue and *(v)* reasonable costs. One technological solution is shaping of Zerodur glass ceramic (Schott Glas, Mainz) which is used for manufacturing precision spherical optics. Since adhesion of HOPG crystals to Zerodur in dependence on surface processing was never tested, it was investigated by coating small blocks with crystals produced by Bourevestnik Inc., Sankt-Petersburg. These crystals are especially suited for covering bended moulds. After polishing (surface defects of 5/3x0.25, DIN 3140) the crystals adhere to the surface, but not after fine sanding (micro roughness $R_Z < 3\,\mu$m). However, the time consuming curving and polishing procedure of Zerodur results in costs of more than 50.000 € for one mould (Berliner Glas KG, Berlin). Therefore, adherence of HOPG crystals to three different plastics was investigated: polymethylmethacrylate (PMMA, $C_5H_8O_2$), a more common mould material for HOPG monochromators, and two high performance plastics which are resistant to photon radiation (SINTIMID and TECAPEEK, Ensinger GmbH, Nufringen). Adhesion to PMMA was proved to be excellent after polishing (diamond suspension, $R_Z = 0.4\,\mu$m) and still reasonable after milling with a diamond face cutter ($R_Z = 1.1\,\mu$m), whereas from the other two materials, only SINTIMID shows reasonable adhesion after high quality polishing ($R_Z = 0.8\,\mu$m). Therefore, a PMMA mould was decided to be produced.

At first, the steps were made as individual rectangular blocks with high accuracy. Furthermore, a mortise was shaped in step 1 to receive the tenons, i.e. step 2 to 6 (cf. Fig. 1). Then the curvature of step 1 was shaped by CNC-moving a hob along X and Z, whereas bending along Y was achieved by the shape of the hob. In the same way, the other steps were shaped by joining them subsequently with step 1, the most sticking out last. The resulting surface roughness was measured to be $R_Z = 0.2\,\mu$m (along X) and $R_Z = 1.8\,\mu$m (along Y), respectively. Curvature measurement of a test sample of step 1 showed deviations in the radius of curvature as well as influence of sample torsion (Fig. 2, above). Improvements in support, fixation, alignment procedure and CNC software resulted in better agreement for the final mould (Fig. 2, below). Finally, the mould was coated with HOPG crystals of several microlayers up to 0.2 mm total thickness (Fig. 3). The overall offset of 0.2 mm can be adjusted by positioning at the beam line, whereas the offset of steps 2 and 3 (cf. Figs. 1 and 2) was compensated by 0.07 mm increase of HOPG thickness. Since the small steps (2 - 6, Fig. 1) didn't show stable adherence, a minimum amount of glue had to be used.

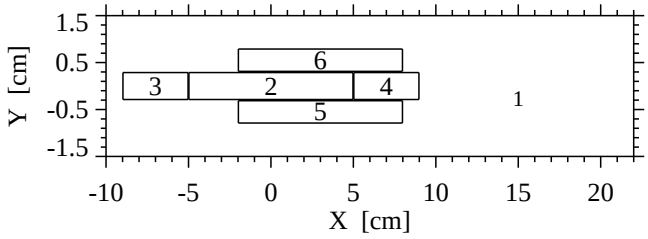

Fig. 1 *Geometry of the stepped monochromator design.*

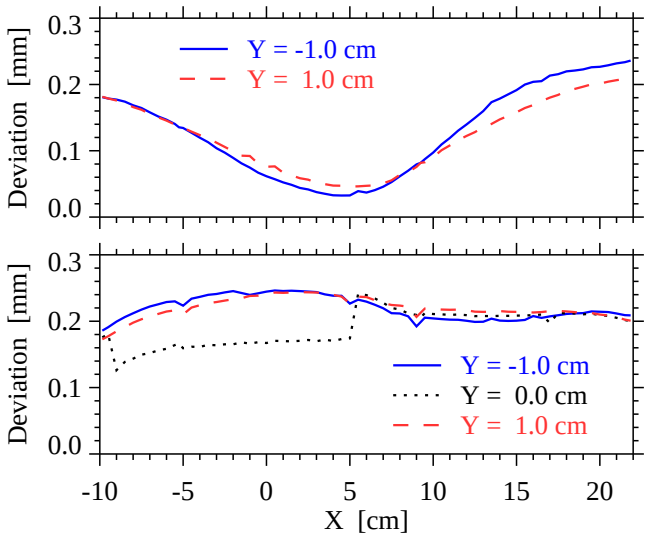

Fig. 2 *Difference between measured and nominal height value of curvature for the test sample of step 1 (above) and final mould (below), respectively.*

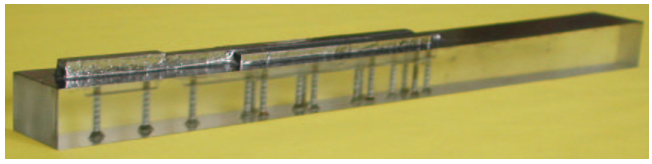

Fig. 3 *Photo of the final monochromator.*

[1] W. Neubert et al., FZ Rossendorf, Wiss.-Tech. Ber. FZR-319 (2001) 41
[2] J. Pawelke et al., FZ Rossendorf, Wiss.-Tech. Ber. FZR-341 (2002) 91

[1] *Kunststofftechnik GmbH, Dresden*

The Influence of Electron Scattering in the Target on the Beam Transmission

H. Müller, W. Neubert, U. Lehnert[1]

The interaction of the electron beam with targets increases the divergence and leads to collisions with the beamline materials producing bremsstrahlung and, to a lower extend, neutrons. According to the demands of radiation protection in the radiation physics cave such beam loss must be less than 5 μA at ELBE. The intended irradiation of cell cultures with quasi-monochromatic channeling radiation requires also a very low background level. These requirements can be fulfilled only by an optimized beam transport to the beam dump. Since beam transport codes usually do not take into account interactions with target materials specific simulations with other transport codes like GEANT become necessary. In our calculations we defined the transmission as the ratio of the number of electrons at the exit of the bending magnet or at the entry of the beam dump, respectively, to the number of electrons started in front of the target. Earlier simulations carried out with GEANT 3.21 [1] have shown that the original beamline design [2] had to be upgrated with an increased beam tube 66 mm in diameter connecting goniometer chamber and bending magnet. Further, an increase of the gap of the original 45^o bending magnet to 90 mm was necesssary. Simulations carried out with targets of carbon (35 and 100 μm thick, with the density of diamond) showed that the above requirements can be fulfilled for this new design for beam energies above 15 MeV only. But the limited power of the dipole magnet allows at 90 mm gap and higher electron energies only deflections less than 45^o. Therefore, the new vacuum chamber was designed for the bending angle of 35^o.

The complete upgrated beamline with the 35^o bending magnet and the beam tubes to the beam dump [4] with additional quadrupol lenses has been implemented into a geometry file for GEANT 4. Instead of the constant magnetic field in the GEANT 3.21 simulations the complete magnetic field chards [2] have been used in the GEANT 4 version. Fig. 1 shows the results of these simulations with incident energies from 5 MeV to 40 MeV. In Table 1 we summarize and compare the results obtained by GEANT 3.21 and GEANT 4.4.1 behind the beam bending magnet. Both code versions show a reasonable agreement at the reference energy of 20 MeV. Slight differences in Table 1 are due to different bending angles and the treatment of the magnetic field. There are considerable differences at lower energies between GEANT 3 and 4 results but both simulations show that beam losses will limit the available beam current, especially at electron energies below 20 MeV.

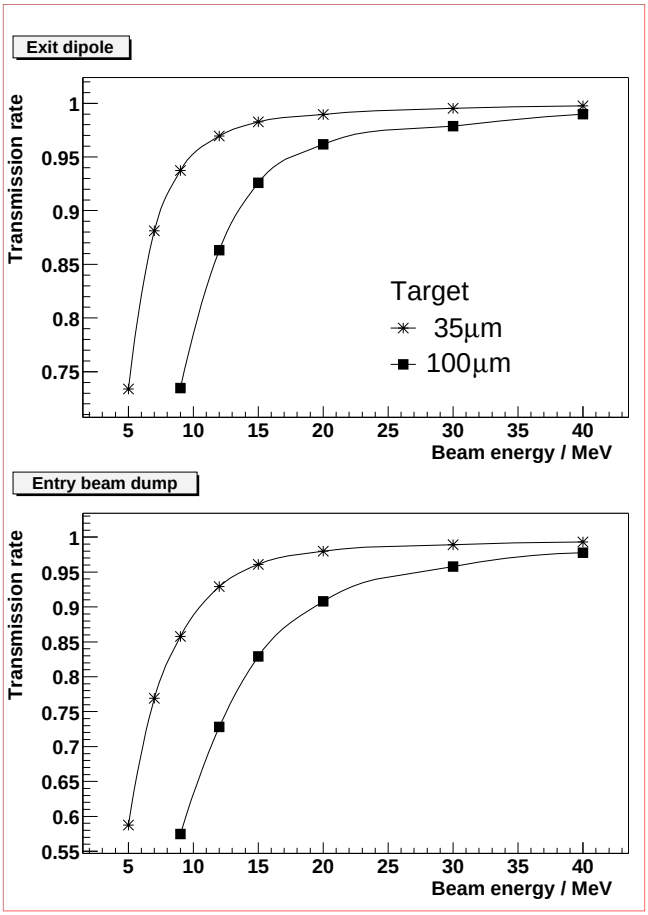

Fig. 1 *Transmission rate for the exit of the dipole (upper panel) and the entry of the beam dump (lower panel) as function of the electron energy obtained from GEANT 4.4.1 simulations.*

Table 1 *Transmission rates for the exit of the dipole magnet calculated by GEANT 4.4 (g4) and GEANT 3.21 (g3). 35 deg bending in g 4 ; 45 deg. bending in g 3.*

GEANT version	g4	g3	g4	g3
d_{target}/μ	35	35	100	100
E_e=7 MeV	0.88	0.76	0.60	0.55
E_e=9 MeV	0.94	0.86	0.73	0.70
E_e=12 MeV	0.97	0.94	0.87	0.86
E_e=15 MeV	0.98	0.97	0.93	0.92
E_e=20 MeV	0.99	0.99	0.96	0.97
E_e=40 MeV	1.00	-	0.99	-

[1] W. Neubert, W. Enghardt, U. Lehnert, E. Müller, B. Naumann, A. Panteleeva, J. Pawelke, Proceedings Monte Carlo 2000 Conference, Lisbon, 23–26 Oct. 2000, p. 123

[2] U. Lehnert, FZ Rossendorf, Wiss.-Tech. Ber. FZR-319 (2001) 18-19

[3] B. Naumann, Berechnung des Strahlungsuntergrundes in der Umgebung der Strahlfänger an der Strahlungsquelle ELBE, Wiss.-Tech. Ber. FZR-345 (2001)

[1] *FZR, Radiation Source ELBE*

Background at the Radiation Physics Beam Line

H. Müller, W. Enghardt

One area of research at the new ELBE facility at the FZR will be devoted to radiobiological experiments with quasimonochromatic X-rays, which are produced by channeling the electrons from the accelerator in crystalline targets. The interaction of the electrons with the target increases the divergence of the electron beam. This enlarges the number of collisions with the beam line materials producing bremsstrahlung and, at sufficiently high energies, also neutrons.

For carrying out experiments with photons the electron beam has to be separated from the X-rays produced in forward direction. This is performed by means of a dipole magnet. Its field map has been calculated [1] using the code Poisson [2]. In order to minimize the background arising from electrons hitting the beam line two quadrupoles are arranged behind the dipole to focus the electron beam on the beam dump. For the correct understanding of the main background sources a Monte-Carlo simulation of the whole beam line starting from the channeling target up to the beam dump is carried out on the basis of the code GEANT4 [2]. The beam profile after the dipole for a point-like electron beam of 50 MeV impinging on a 100 μm thick diamond target is shown in the left panel of Fig. 1. In the right panel the focusing effect of the two quadrupoles is demonstrated. At the entry of the beam dump the beam is much narrower than at the exit of the dipole.

Fig. 2 shows the radial dependence of the flux of particles backscattered by the beam dump in the upper panel, while the lower panel shows the energy spectra. Compared to earlier calculations [4] where a beam diameter of 8 cm was assumed the present calculations yield a reduced background. This can be understood by the smaller beam diameter. The majority of electrons hits the dump material in a larger distance from the entry due to the cone-like opening of the beam dump (see [4]).

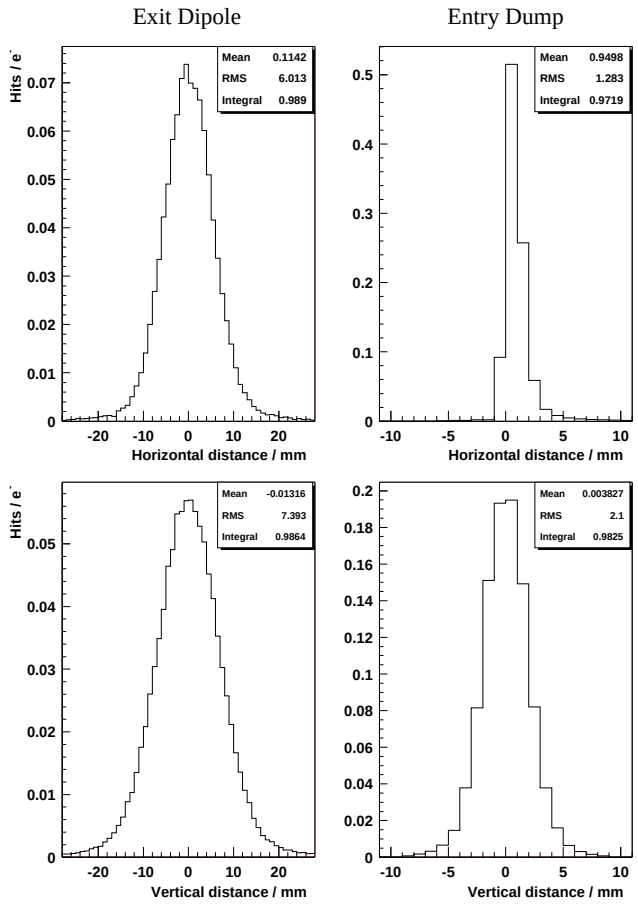

Fig. 1 *Profile of a 50 MeV electron beam in horizontal (upper panel) and vertical (lower panel) direction at the exit of the dipole (left panel) and the entry of the beam dump (right panel).*

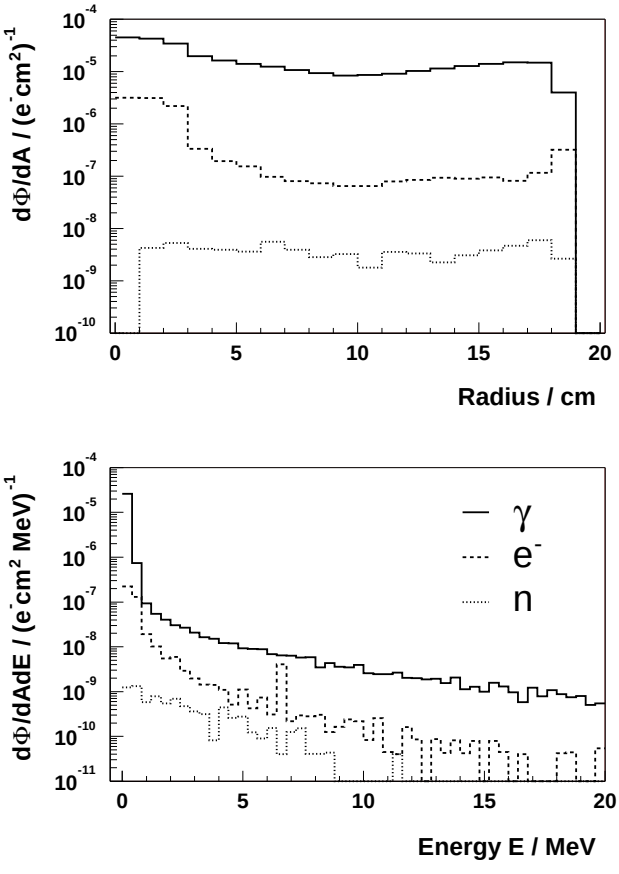

Fig. 2 *Radial flux of background particles escaping the beam dump in backward direction as function of the radius (upper panel) and the corresponding energy dependence averaged over the whole area (lower panel).*

[1] U. Lehnert, private communication
[2] J.H. Billen, LA-UR-06-1834, Los Alamos (1998)
[3] http://wwwinfo.cern.ch/asd/geant4/geant4.html
[4] B. Naumann, Berechnung des Strahlungsuntergrundes in der Umgebung der Strahlfänger an der Strahlungsquelle ELBE, Wiss.-Tech. Ber. FZR-345 (2001)

Shielding Calculations for an X-Ray Laboratory

U. Reichelt, J. Henniger[1], W. Neubert, J. Pawelke

In preparation of projected experiments with X-rays at the ELBE facility of the FZR, it is intended to build up an appropriate laboratory. For dimensioning the radiation shielding a transport simulation had to be done.
The X-ray tube ISOVOLT 320/13 made by Agfa NDT Pantak Seifert will be used as source. The maximal tube voltage is 320 kV and the maximum anode current is 13 mA [1]. The exit window collimates the photons to a cone with 20 degrees opening angle. The laboratory will be installed in the ELBE experimental hall. The outline is shown in Fig. 1. Two of its walls consist of heavy concrete. They are at least two meters thick. The other walls are made of 2.8 or 10 cm thick lead panels. The positioning of the horizontal emitting source assures that the hole radiation cone impinges at the left concrete wall. Thus no unscattered photons will leave the cave through the top.

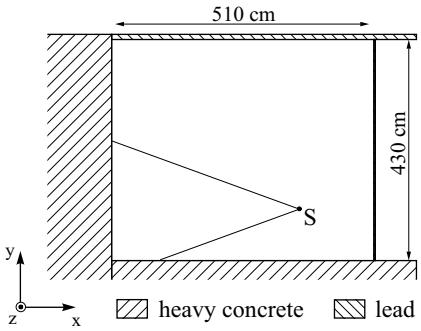

Fig. 1 *Topview of the cave, position of x-ray tube 'S' and its radiation cone*

The calculations can be devided into two parts. First the X-ray spectrum was determined by bombarding a tungsten target with 320 keV electrons. The spectrum of bremstrahlung photons emitted inside the radiation cone was calculated by means of Geant3. Its results were the source term of the second simulation part, where photon transport was performed with the Monte Carlo code AMOS [2], developed at the TU Dresden. This program is implemented on a straight probabilistic base. All cross section functions are represented by cumulated probability density functions (cpdf). Therefore 10^8 particle histories could be simulated and results of low statistical error were achieved with a normal effort of computing power. The conversion factors from ICRP 51 [3] were used to transform the spectral photon flux density to effective equivalent dose rate. For this purpose frontal irradiation was conservatively assumed.
A first simulation was done without shielding the ceiling of the laboratory. The dose distribution at a height of 2.80 meters shows a maximum of 103 mSv/h (Fig. 2), what exceeds the allowed limit by several orders of magnitude. Therefore a ceiling of 1cm lead was added in a second simulation. Because of large incident angles and low energy values of backscattered photons, no transmission was determined behind all lead shieldings with the exception of areas, where the lead shieldings are mounted to the concrete walls. The larger mean free path in concrete results in backscattered photons, which bypass the lead shielding. This fact explains the detected dose rates along all edges of lead to concrete what is shown in Fig. 3.
The physical problem, wich difficulty is in its large dimension, could be solved with the used Monte Carlo code. The results evince that one centimeter lead for the ceiling will be enough to allow the access also during experiments. Additional small shieldings along the edges should be installed.

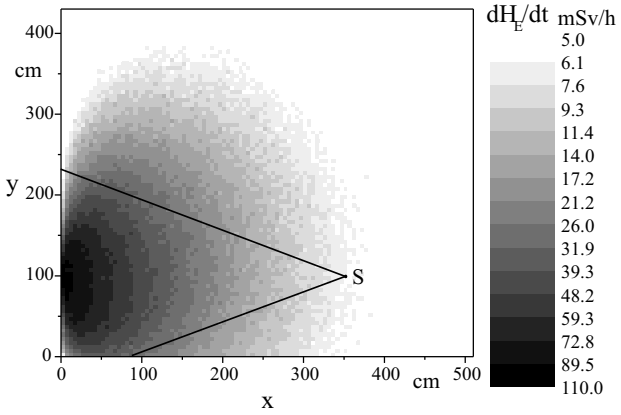

Fig. 2 *Dose rate distribution at the unshielded ceiling (height 2.80 m; at: 320 kV, 13 mA)*

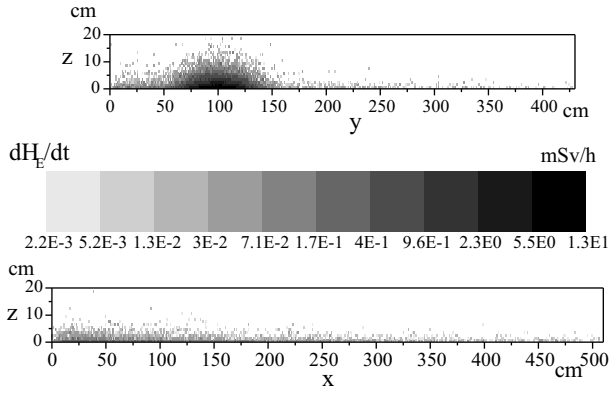

Fig. 3 *Dose rate distribution at the sides of the 1 cm lead shielded ceiling along the left (upper graph) and lower (lower graph) concrete wall of Fig. 1*

[1] Bedienungsanleitung ISOVOLT 160/225/320/450HS, Agfa NDT Pantak Seifert, 2002
[2] J. Henniger, AMOS - ein multivalent nutzbares Programmsystem zur Berechnung von Strahlungstransportproblemen, Strahlenschutz: Physik und Messtechnik, Band 1, Verlag TÜV Rheinland, S.145-150, 1994
[3] ICRP 51, Data for Use in Protection Against External Radiation, Annals of the ICRP, Vol.17, No.2/3, 1987

[1] *Institute for Radiation Protection Physics, TU Dresden*

Comparison of Bremsstrahlung Distributions with Results from Monte-Carlo Codes

W. Neubert, H. Müller

Bremsstrahlung is frequently an undesired background in many applications at electron accelerators. One way to identify the sources of bremsstrahlung and to minimize this disturbance are proper simulations with electro-magnetic transport codes which take into account the setup geometry.

Here we analyze the reliability of two Monte-Carlo codes by comparison of simulation results with experimental data. In ref. [1] double differential bremsstrahlung distributions at $\Theta = 0^o$ and 0.62^o with respect to the electron beam with kinetic energies of 2.72, 4.54 and 9.66 MeV were obtained from thin targets of Be, Al and Au. We chose the data set for 9.66 MeV because this energy is close to the energy now available at the accelerator ELBE. The simulations were performed for the solid angle acceptance determined by the experimental setup in ref. [1].

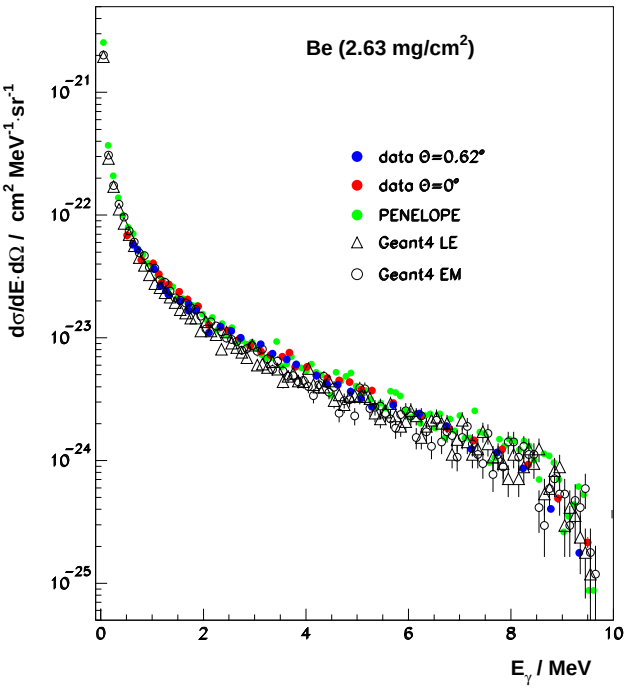

Fig. 1 *Experimental and simulated bremsstrahlungs distribution induced by 9.66 MeV electron on Berylliums.*

Overall, the agreement between the experimental data and the simulation results obtained with PENELOPE (version 2001) is excellent within the error bars. Simulations with GEANT 4 (version 5.0) [2] were performed for both the low-energy (LE) and for the standard electromagnetic versions (EM). Both results are also in good agreement both with that from PENELOPE and with the experimental data. We mention that the former discrepancies between the experimental data of aluminium and the corresponding simulations with the low-energy version of GEANT 4.4.1 [4] are not observed with the latest release 5.0 of GEANT 4.

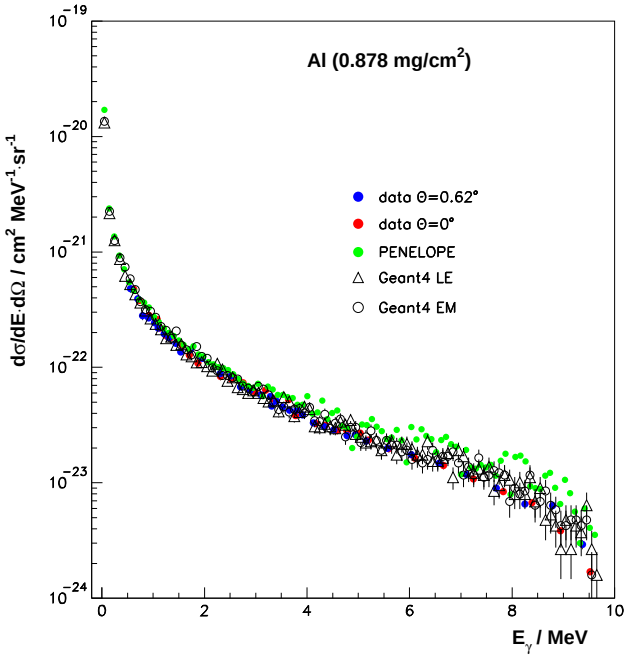

Fig. 2 *The same for Aluminium.*

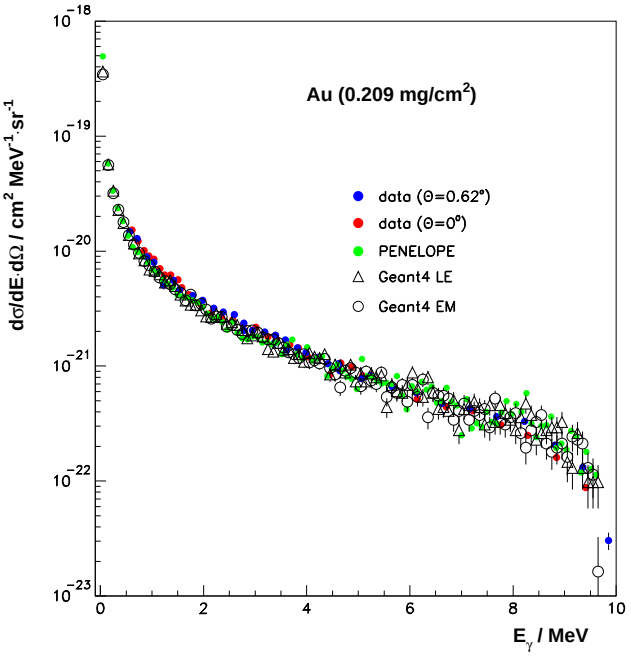

Fig. 3 *The same for Gold.*

[1] N. Starfelt and H.W. Koch, Phys. Rev. 102 (1956) 1598
[2] http://wwwinfo.cern.ch/asd/geant4/geant4.html
[3] F. Salvat et al., PENELOPE, A code System for Monte Carlo Simulations of Electron and Photon Transport, Workshop Proceedings Issy-Ies-Moulineaux, France, 5-7 Nov. 2001, Data Bank OECD, Nuclear Energy Agency
[4] W. Neubert, talk at the MCNEG user meeting, Stoke-on-Trent, England, April 22-23, 2002

Calculation of Photon-Induced Auger Transitions in Tc and Re

W. Neubert, W. Enghardt

The code package PENELOPE [1] allows to simulate the atomic relaxation process of singly ionized atoms with an initial vacancy in the K or L subshells for atoms from Z = 6 to Z = 92. The necessary transition probabilities for the simulation of radiative and non-radiative transitions are taken from the EADL data base [4] with the adoption of experimetal X-ray energies from ref. [3].

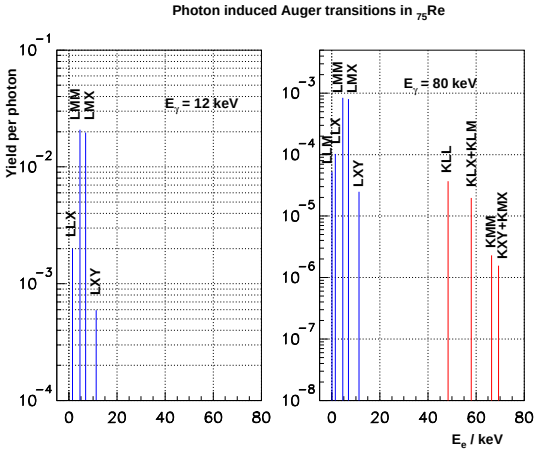

Fig. 1 *Auger electron spectra calculated for photon energies below (left panel) and above (rigth panel) the K-absorption edge of Rhenium.*

The photoelectric absorption in a given medium is simulated by means of the corresponding cross sections which determine the shell that has been ionized. The program was modified such that only the interaction events with non-radiative transitions were registered. This allows to survey the Auger electron spectra within the complex electron emission like photoelectrons and electrons from the Compton scattering. Special flags were set to proceed certain Auger cascades after photoabsorption using a special label code, see [1]. Here we show the emission spectra of Tc and Re. Both elements are of special interest as constituents of metallo-organic compounds which can be attached closely to the DNA. Table 1 shows a comparison of transition energies in Tc. The results obtained with PENELOPE are in good agreement with that from refs. [4, 2]. There are only small differences for transitions like LMX, LXY and LLX where the X and Y contributions are not well defined. The deterministic [4] and the MC calculations [2] assume vacancy production accompanied by the radioactive decay of ^{99m}Tc whereas PENELOPE assumes randomly distributed single vacancies in the K and L subshells. Auger electron spectra of Rhenium induced by two fixed photon energies are shown in fig. 2. The excitation function of transitions related to initial vacancies in the L subshells show that their yield follow closely the energy dependence of the photo-absorption coefficients.

Table 1 *Energies of Auger transitions in Technetium. The first column gives the Auger process, where the first letter denotes the shell with the vacancy before the Auger transition, the second and third letters indicate where the new vacancies are created, where X or Y denote shells above the specified ones.*

Transition type	Energy PENELOPE	Energy Stepanek [4]	Energy Howell [2]
KLL	15.4 keV	15.4 keV	15.3 keV
KLX	17.8 keV	17.8 keV	17.8 keV
KXY	20.3 keV	20.2 keV	
LMM	2.06 keV	2.06 keV	2.05 keV
LMX	2.41 keV	2.33 keV	2.32 keV
LXY	2.76 keV	2.64 keV	2.66 keV
LLX	146.0 eV	106.0 eV	

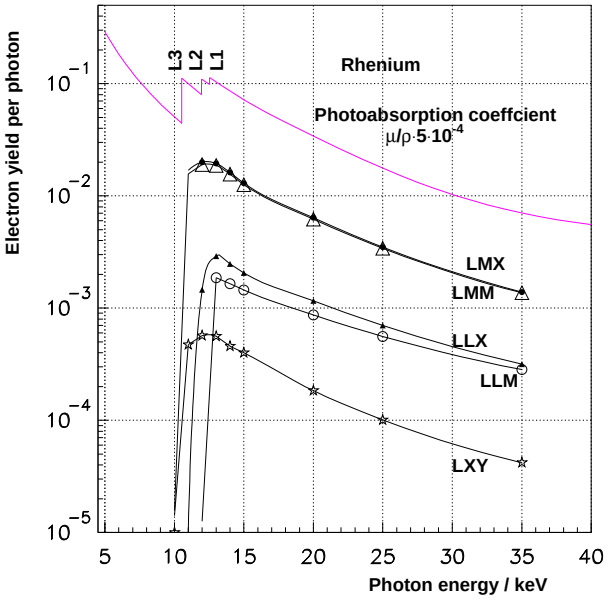

Fig. 2 *Excitation function of transitions related to L subshell vacancies. The photon energies are larger than the L_3 absorption edge.*

[1] F. Salvat et al., PENELOPE, A code System for Monte Carlo Simulations of Electron and Photon Transport, Workshop Proceedings Issy-Ies-Moulineaux, France, 5 - 7 Nov. 2001, Data Bank OECD, Nuclear Energy Agency
[2] S.T. Perkins et al., Tables and graphs of atomic subshell and relaxation data from LLNL evaluated atomic data library, Vol. 30, UCRL-50400 (Livermore, CA, 1991)
[3] J.A. Bearden and A.F. Burr, Rev. Mod. Phys. 39 (1967) 125
[4] J. Stepanek, Med. Phys. 27 (2000) 1544
[5] R.W. Howell, Med. Phys. 19 (1992) 1371

Auger Electron Emission in Tc: Photon Induced versus Radioactive Decay

W. Neubert, W. Enghardt

The method described in [1] allows Auger electron spectra for monoenergetic photons to be calculated. Here we consider the more realistic case of a complex X-ray spectrum delivered by the commercial X-ray tube ISOVOLT/320-2. The emission spectrum was simulated by GEANT 3.21 for 320 keV electron impact on a tungsten anode and for an emission angle of 40^o. The obtained spectrum in Fig. 1 shows the prominent K_α and K_β lines of tungsten located on the continous bremsstrahlung background. The reliability of this calculation was verified by the good agreement of the measured X-ray spectrum with the corresponding simulation for 100 keV.

The intense characteristic X-rays of tungsten are far above the K-absorption edges of Tc so that vacancies in both the K and L subshells can be created. Auger cascades induced by this X-ray spectrum were calculated for fixed energies in steps of 7 keV, weigthed by the corresponding X-ray yields from Fig. 1 and then they were summed up. This spectrum of Auger transitions obtained without consideration of the electron propagation in the thin slab of Tc (0.1 μm) is shown in Fig. 2. In this figure the intensities are compared with the results for the radioactice decay of ^{99m}Tc taken from ref. [3]. These deterministic calculations utilize the same data base EADL [4] which is implemented in the Monte-Carlo code PENELOPE. The relative intensities of Auger transitions related to initial vacancies in the K and L subshells are similar. But the absolute intensities for the external irradiation of any isotope of Tc by X-rays are about two orders of magnitude less compared with those from the radioactive decay although the relevant photon energies are comparable, i. e. 142.7 keV of the isomeric M4 transition in ^{99m}Tc. If any isotope of Tc is attached to biological structures of interest and K- and L-shell Auger cascades are induced by external photon irradiation then the yield of these Auger electrons per photon is essential lower compared with the case that it is replaced by the radioactive ^{99m}Tc.

The expected enhancement of the RBE of photons by suitable atoms becomes ineffective due to the reduction via the photoabsorption cross sections. The higher the photon energy the lower the Auger electron yields. Since the yield of Auger cascades is strongly coupled to the photoabsorption coefficients, the most promising scenario for the increase of the RBE of photons are photon energies around the L absorption edges which can produce vacancies both in the M- and in the higher subshells followed by Auger cascades of very low energy.

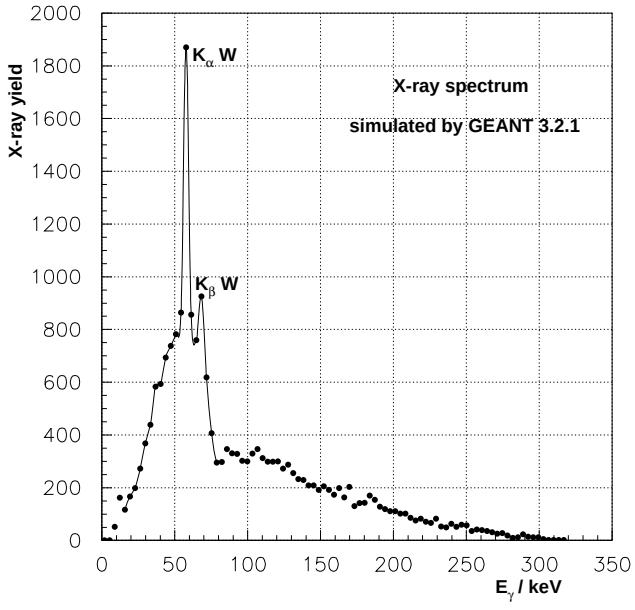

Fig. 1 *Simulated emission spectrum of a X-ray tube.*

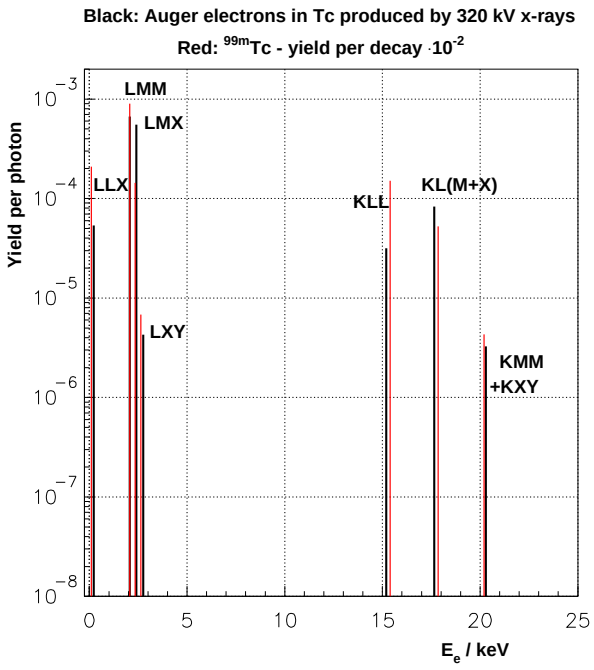

Fig. 2 *Comparison of the photon-induced Auger transitions in Tc with those from the radioactive decay of ^{99m}Tc.*

[1] W. Neubert et al., This Report, p. 73

[2] F. Salvat et al., PENELOPE, A code System for Monte Carlo Simulations of Electron and Photon Transport, Workshop Proceedings Issy-Ies-Moulineaux, France, 5-7 Nov.2001, Data Bank OECD, Nuclear Energy Agency

[3] J. Stepanek et al., Acta Oncologica 35 (1996) 863

[4] S.T. Perkins et al., Tables and graphs of atomic subshell and relaxation data from LLNL evaluated atomic data library, Vol. 30, UCRL-50400 (Livermore, CA, 1991)

Dose Distributions of Photon-Induced Secondary Electrons in Tc

W. Neubert, W. Enghardt

The code package PENELOPE [1] is to our knowledge the only tool which allows to propagate electrons with energies down to 100 eV in arbitrary media. MCNP4 and EGS4nrc are restricted to about 1 keV. This low tracking threshold allows to investigate the complex atomic relaxation process following single vacancies in the K and L subshells. We chose Technetium which is characterized by a balanced competition between radiative and non-radiative transitions. Moreover, Tc is of biochemical interest because it can be inserted into special organic compounds.

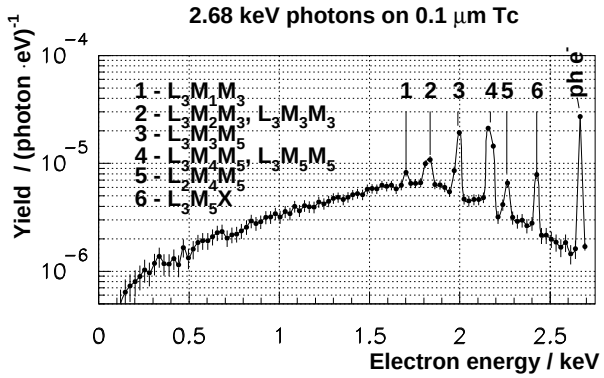

Fig. 1 *Simulated Auger electron spectrum induced by photons equal to the L_3 absorption energy.*

Fig. 1 shows the simulated spectrum of secondary electrons produced in a thin layer of Tc irradiated by photons. This figure demonstrates the increasing complexity of the spectrum. Photons with an energy equal to the L_3 absorption edge produce a proper Auger electron spectrum with a single contribution of photoelectrons. A slight increase of the photon energy above the L_1 absorption energy leads to further disturbing contributions of L-shell photoelectrons and of such ones produced by a secondary process, i.e. by the $L_{\alpha,\beta}$ radiative transitions, both placed on a complex distribution of backscattered electrons.

In order to calculate the corresponding dose distributions we chose a cylindrical water phantom (10 μm thick). First of all we assumed a direct impact of 2.05 keV electrons which corresponds to the average energy of the LMM Auger transition type in Tc [2]. Such electrons provide a high local energy deposition of about 10^8 eV/cm $\cdot$ e$^-$ within a slab thickness ≤ 0.5 μm. Then the phantom was covered by 0.1 μm Tc in order to simulate the energy deposition by primary photons and induced Auger transitions. The assigment of low-energy LMM/LMX Auger transitions was performed by means of the label code [1] which allows also to score the corresponding dose distributions. As shown in fig. 2 the tail of this distribution corresponds to the known range of these electrons in water [2]. But the maximum dose released by photon induced Auger electrons is about two orders of magnitude less compared with those from the direct impact of equivalent electrons. A similar behaviour was found for the KLL Auger transition of an average energy of 15.3 keV. An insignificant enhancement of the dose with respect to that from the primary photons was found only within some sub-μm on the front side of the phantom.

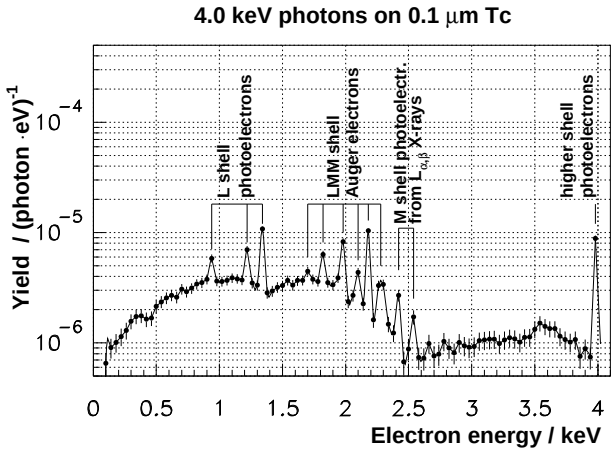

Fig. 2 *The same as fig. 1 but for 4 keV incident photons.*

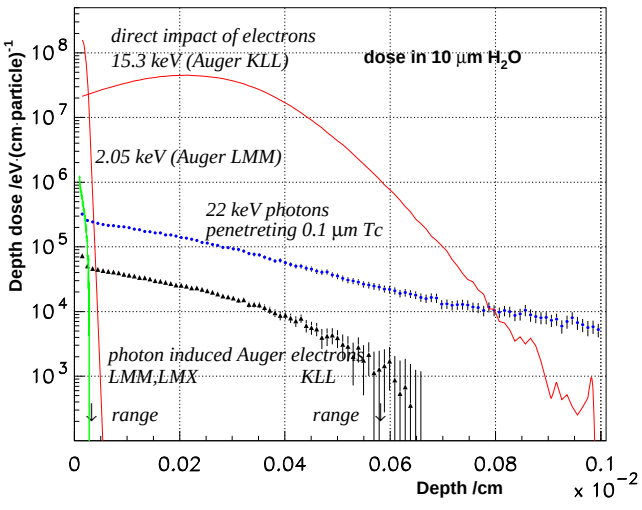

Fig. 3 *Comparison of depth dose distributions of selected Auger transitions (direct impact and photon induced).*

[1] F. Salvat et al., PENELOPE, A code System for Monte Carlo Simulations of Electron and Photon Transport, Workshop Proceedings Issy-Ies-Moulineaux, France, 5-7 Nov.2001, Data Bank OECD, Nuclear Energy Agency

[2] R.W. Howell, Med. Phys. 19 (1992) 1371

Scatter Correction for In-Beam PET Monitoring of Heavy Ion Therapy [G]

F. Pönisch, W. Enghardt

The process of scattering of the annihilation gamma quanta reduces the quality of PET images. About 30 % of the true coincidences registered during *in situ* PET monitoring of head and neck carbon ion tumour irradiations are influenced by Compton or Rayleigh scattering. These physical processes may deteriorate the correspondence between the source and the reconstructed radioactivity distribution especially in highly inhomogeneous regions of the human body like the head and neck. Therefore, an attenuation and scatter correction algorithm is necessary for quantitative PET imaging [1]. This algorithm has been successfully applied for the reconstruction of PET data sets generated by means of Monte Carlo methods and obtained from measurements during phantom experiments [1]. In 2002 the feasibility of the iterative scatter correction algorithm has been demonstrated for the reconstruction of measured as well as model-based calculated patient listmode data.

The scatter correction algorithm requires the knowledge of the density information within and nearby the positron camera field of view. This is derived from the X-ray computed tomograms (CT) of the patient (taken for treatment planning purpose) and the head rest CT [2]. This attenuation map is the basis of the calculation of the attenuation correction factors along each line of response (LOR). The number of events measured for each LOR are corrected for the individual detector efficiency and the length of the emission line within the image space. Additionally, random events are subtracted from prompt events. The classical Maximum Likelihood Expectation Maximization algorithm of Shepp and Vardi [3] estimates the expectation step by computing the ray sums in each projection. We modified this procedure by applying the attenuation correction factors to the forward projection and adding furthermore, the scattered components. The latter is calculated according to the approximation of Watson [4], the Single Scatter Simulation (SSS). The SSS algorithm neglects multiple scatter, calculates the scatter contribution to a certain LOR for a finite number of discrete points of the scatter volume only and does not take into account the efficiencies of the individual crystals. Therefore, the total number of scattered events obtained from the calculation has to be normalised to the number of acquired coincidences. For this purpose, we calculate the global scatter fraction (SF) by means of an additional Monte Carlo (MC) simulation. The simulation uses the activity distribution of the previous iteration step and the information of the attenuation map. The MC code has been optimised for accuracy and execution time. The number of histories has been chosen that the statistical error in the calculated SF is less than 0.3 %. The scatter correction reconstruction algorithm is rather complex and demands high computational effort, but it has the advantage that no assumption of the shape of the activity and scatter distribution is made.

The reliability of the proposed algorithm for the particular application in limited angle PET has been shown for patient data. Figure 1 shows evident improvements in the reconstructed PET image. Scatter correction drastically reduces the spurious activity occurring laterally to the beam path as it is revealed by comparing the images of figure 1. Furthermore, the shape of the contour lines in the central part of the image is nearly identical. That means, that the scatter correction algorithm eliminates the Compton scattering in the image and preserves the true β^+-activity distribution.

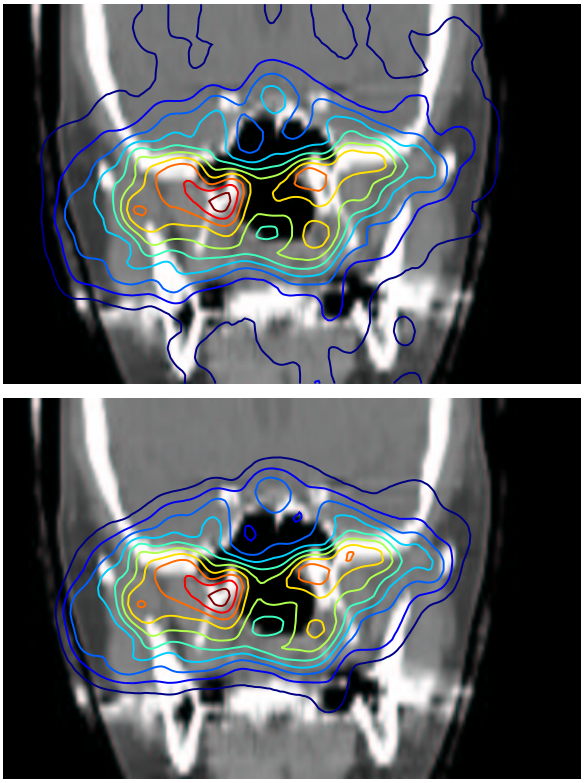

Fig. 1 *Frontal slice of the head CT of a patient (grey scaled in the background). Comparison of the measured PET activity distributions for a beam portal that is typical for treating skull base tumours. The beam enters the patient from the right side (left on the figures). The β^+-activity are reconstructed with attenuation correction (top), with attenuation and scatter correction (bottom).*

[1] F. Pönisch and W. Enghardt, FZ Rossendorf, Wiss.-Tech. Ber. FZR-341 (2002) 99
[2] F. Pönisch et al., FZ Rossendorf, Wiss.-Tech. Ber. FZR-319 (2001) 95
[3] L.A. Shepp, Y. Vardi, IEEE Trans. Med. Imag. MI-1 (1982) 113
[4] C.C. Watson et al., in Three-Dimensional Image Reconstruction in Radiation and Nuclear Medicine (1996) 255-268

The Time Dependence of the γ-Ray Intensity Seen by an In-Beam PET Monitor [E, G]

K. Parodi, P. Crespo, W. Enghardt, T. Haberer[1], J. Pawelke, D. Schardt[1]

The design study of the new generation in-beam PET scanner to be developed and installed at the dedicated ion beam tumour therapy facility of Heidelberg, Germany [1], demands a deep understanding of physical processes affecting in-beam PET acquisition. The current experience in the monitoring of carbon ion therapy at GSI Darmstadt shows that techniques well established in radiotracer imaging may fail in the non-conventional case of in-beam PET therapy monitoring. In fact the data acquired by the in-beam positron camera during particle extraction (spill) from the GSI synchrotron are corrupted by a high noise level. They are therefore discarded for tomographic reconstruction. Previous investigations have suggested the reason of high noise to be random concidences not properly corrected for during beam extraction. The standard random correction technique implemented by the manufacturer of our PET data acquisition system (CTI PET Systems, Knoxville, TN, USA) is based on subtraction of delayed (by 128 ns) from prompt coincidences. The failure of the correction during particle extraction is thought to be due to a non-stationary (in the sub-μs scale) γ-background originating from nuclear reactions induced by the beam and hence following the time microstructure of the carbon ions [2]. The time dependence may result in a reduction of delayed coincidences affecting the proper correction for the random coincidences detected in the prompt window. This conjecture has been supported by previous in-spill measurements of time correlation between the γ-rays produced in ^{12}C irradiation of organic matter and the synchrotron radiofrequency (RF) using a GSO scintillating crystal (2 cm radius and 2.5 cm thickness) coupled to a fast PMT [3]. In the presented experiment an improved electronics was set-up in order to add photon energy discrimination to the time information. A further record of the spill number was introduced in order to perform dynamic acquisition and establish the relationship between the single photons detected by the GSO crystal and the coincidences simultaneously recorded by the positron camera during particle extraction. The same experimental configuration of [3] was chosen. Monoenergetic carbon ion beams (energy: $88.83 - 426.11\,A$MeV, intensity: $1{\cdot}10^8{-}4{\cdot}10^6$ ions per 2 s spill) were completely stopped in blocks of PMMA ($C_5H_8O_2$) placed at the isocentre of the treatment unit in the middle of the positron camera field of view. The GSO detector was set perpendicular to the beam at the same distance (41 cm) as the positron camera heads from the isocentre. The experiment confirmed a time correlation of the γ-background seen by the in-beam PET scanner with the RF signal (Fig. 1) and hence with the previously measured ion beam microstructure [2]. The physical interpretation of the time distribution has been already discussed in [3]. The data analysis has addressed the comparison between (*i*) the calculated prompt and delayed coincidence rate induced by single γ-rays modulated in time according to the GSO data and (*ii*) the "beam-induced" (i.e. not related to β^+-activity) prompt and delayed rate extrapolated from the measured PET data. The rather good agreement (Fig. 1, right) supports the explanation of random correction failure due to a γ-background correlated in time with the beam microstructure. A more detailed analysis will be reported soon in a forthcoming paper. This work will be the basis for a new data acquisition concept for in-beam PET.

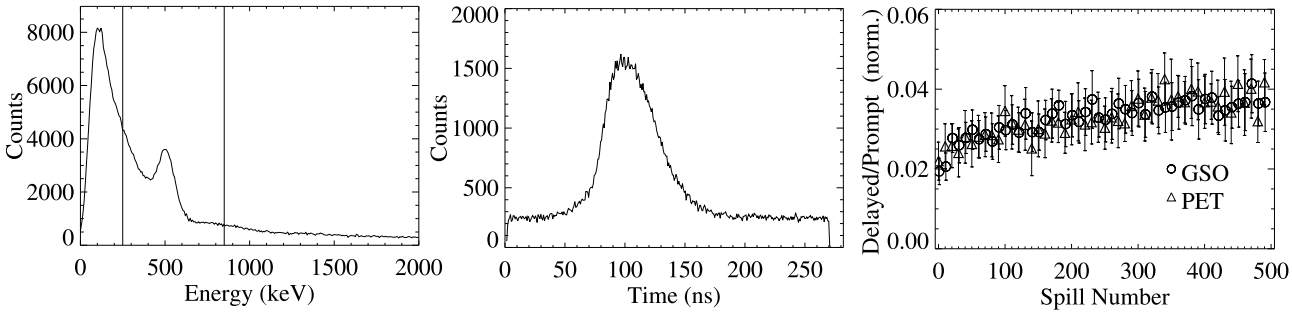

Fig. 1 *Energy (left) and γ-RF time (middle) spectrum detected by the GSO crystal during 500 spills of ^{12}C irradiation at 280.48 AMeV energy (RF period of 282.4 ns) and $8.5{\cdot}10^6$ ions/spill intensity. Only the time distribution of photons with energy in the marked $250-850$ keV window accepted by the positron camera is shown. Right: Ratio of the "beam-induced" delayed and prompt coincidence rate deduced from the GSO and PET data in dependence of the extracted spill. The delayed to prompt ratio from the GSO data was normalised to the average delayed to prompt ratio extracted from the PET data.*

[1] K. D. Gross and M. Pavlovic (eds), Proposal for a dedicated ion beam facility for cancer therapy, GSI Darmstadt, 1998
[2] K. Parodi et al., FZ Rossendorf, Wiss.-Tech. Ber. FZR-319 (2001) 97
[3] K. Parodi et al., FZ Rossendorf, Wiss.-Tech. Ber. FZR-341 (2002) 103

[1] *Gesellschaft für Schwerionenforschung Darmstadt*

The Quantification of the Mechanical Deformation of the Rotating Double Head PET Scanner at the ^{12}C Ion Therapy Facility at GSI Darmstadt [B,G]

F. Fiedler, M. Sobiella, W. Enghardt, F. Mönsters[1]

For treating patients in a sitting position at the horizontal beam of the ion therapy facility at GSI Darmstadt a dedicated patient chair has been installed [1]. In order to monitor these irradiations by means of positron emission tomography (PET) the PET gantry has been completely rebuilt [2], which allows now the detector heads to be rotated around the beam axis. The two detector heads with a total mass of 120 kg are mounted on a turnable support. This leads to a deformation of the PET gantry dependent on the rotation angle. The deformation results in a displacement of the crystal positions in comparison to those, which are expected when assuming a rigid body rotation. Furthermore, it has to be supposed that the axis of rotation slightly deviates from the isocentre. Moreover, minor deviations in the parallelism between the axis of rotation and the appropriate axis of the treatment room coordinate system cannot be excluded. In order to obtain a spatially correct superposition of the in-situ PET measurement onto the planning X-ray computed tomograms, which is mandatory for a correct PET data evaluation, we present here a procedure for determining the crystal positions in dependence on the PET gantry angle.

The crystal positions are known in the room coordinate system at 0 deg. It is assumed that the detectors itself behave like rigid bodies during the rotation. Thus the tracking of at least three non-collinear points fixed on the heads during the rotation will give the necessary information to calculate the crystal positions for each angle. These measurements have been performed using a laser tracker.

For this on each head four reference points were defined by means of fastening sphere mounts, which magnetically fix the retroreflectors for laser tracking (fig. 1). The relative accuracy for tracking one point is ± 10 ppm. The measurement was proceeded in steps of 10 deg. Each position was measured twice, moving the gantry clockwise and anticlockwise. The accuracy of setting the angles was ± 0.01 deg, leading to absolute positioning accuracy of ± 0.07 mm according to the distance of the retroreflectors from the axis of about 400 mm.

The results depicted in fig. 2 clearly indicate that a considerable angle dependent deviation between the positions of the detector heads measured and those calculated under the assumption of an ideal rotation is observed. This requires an appropriate correction of the crystal coordinates within the tomographic reconstruction algorithm.

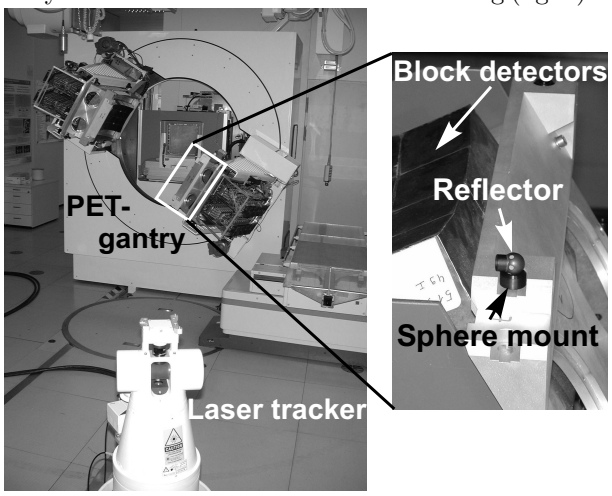

Fig. 1 *The measurement setup for quantifing the mechanical deformation of the PET gantry.*

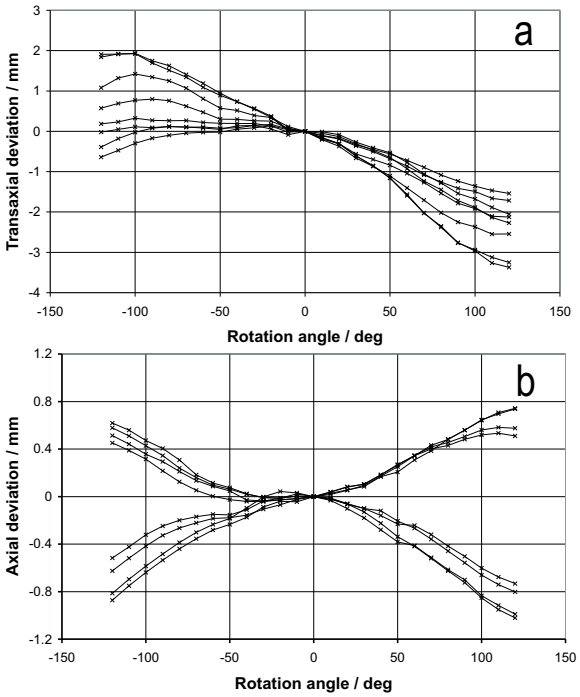

Fig. 2 *The measured deviations of the reference points mounted on the detector heads from the positions deduced from a rigid body rotation.*
a) Deviations within transaxial planes, i.e. perpendicular to the beam.
b) Deviations in axial direction, i.e. parallel to the beam direction.

By means of tracking the positon of four points for each detector head the intrinsic head deformation could be assessed. Maximum deformations along the edges and the diagonales of the detector heads of 0.08 mm and 0.27 mm, respectively, indicate that the influence of the intrinsic head deformation on the crystal positions can be neglected.

[1] P. Heeg et al., GSI, Scientific Report (2000-1) 167
[2] W. Enghardt et al., FZ Rossendorf, Wiss.-Tech. Ber. FZR-319 (2001) 93

[1] *sigma3D GmbH, Gladbeck*

Nuclear Reaction Cross Sections for the Assessment of Positron Emitter Generation by Therapeutic Irradiations with ^{4}He Beams [B, E, G]

F. Fiedler, K. Parodi, W. Enghardt

At the clincal ion therapy facility that will be installed at Heidelberg a variety of ion beams with atomic numbers $1 \leq Z \leq 8$ will be available. Irradiation quality assurance by means of positron emission tomography (PET) is based on the comparison of the β^+-activity distribution predicted from the treatment plan with that measured during the irradiation. Since the β^+-activity distributions strongly depend on the projectile the algorithms developed for carbon therapy [1] has to be extended to other ion beams. To predict the probability of positron emitter generation via nuclear fragmentation reactions, the cross sections for a variety of reaction channels have to be known. Unfortunately, with the exception of proton beams, there is a considerable lack of experimental data in the therapy relevant energy range. Therefore, experimental data have to be completed by model predictions. Here we report on ^{4}He beam induced nuclear reactions since a ^{4}He beam may be of considerable therapeutic interest. A ^{4}He beam has nearly the same radiobiological characteristics as a proton beam but it is superior to protons in respect of lateral scattering. To predict the partial cross sections for reactions with β^+-emitters in the exit channel the code of Silberberg and Tsao (Cross Section Code, [2]) has been applied. It is based on the model of Silberberg and Tsao [3]. This is a semiempirical cross section formula for proton-nucleus reactions. Furthermore the model considers special cases like α- and peripheral reactions. The used formula is:

$$\sigma = \sigma_0 f(A) f(E) e^{-P\Delta A} e^{(-R|Z-SA+TA^2|^\nu)} \Omega \eta \xi$$

where σ_0 is the normalisation factor for the cross section, $f(A), f(E)$ are correction factors for products from heavy targets with atomic number $Z_T > 30$, $exp(-P\Delta A)$ takes into account the difference of target and product mass, the factor $exp(-R|Z - SA + TA^2|^\nu)$ gives the statistical distribution of cross sections for the production of various isotopes of an element of atomic number Z in dependence on mass number A, Ω is a factor related to the nuclear structure, η is the nuclear pairing factor and ξ is a factor for light evaporation products. For nucleus-nucleus reactions a scaling was done according to [4] and [1]. The model reproduces the experimental values for light target nuclei as ^{12}C (fig. 1) and ^{16}O, as the main components in tissue in a satisfactory way (tab. 1). However, even heavier target nuclei, e.g. phosphorus and calcium as constituents of bone has to be taken into account.
In these cases, experimental data are not available and the model predictions have to be relied on (fig. 2).

Energy / AMeV	Target	Fragment	Experiment σ / mb	Absolute error / mb	Calculation σ / mb	Ref.
600	^{12}C	^{11}C	46.2	0.7	43.9	[5]
600	^{12}C	^{10}C	2.1	0.2	1.9	[5]
600	^{14}N	^{13}N	10.5	0.3	17.1	[5]
600	^{14}N	^{12}N	0.9	0.1	2.0	[5]
600	^{14}N	^{11}C	19.8	0.3	19.8	[5]
600	^{14}N	^{10}C	1.6	0.2	0.9	[5]
600	^{16}O	^{15}O	50.3	0.8	49.2	[5]
600	^{16}O	^{14}O	3.1	0.3	2.7	[5]
600	^{16}O	^{13}N	6.8	0.3	5.7	[5]
600	^{16}O	^{11}C	15.8	0.5	16.7	[5]
600	^{16}O	^{10}C	1.8	0.2	0.8	[5]
230	^{16}O	^{15}O	46.4	3.0	45.1	[6]
230	^{16}O	^{13}N	6.8	0.5	5.9	[6]
230	^{16}O	^{11}C	18.5	0.9	17.0	[6]
230	^{27}Al	^{18}F	12.5	0.5	9.7	[6]
95	^{12}C	^{11}C	58.1	2.1	43.9	[7]
230	^{12}C	^{11}C	49.4	1.8	43.9	[7]

Tab. 1 *Comparison between experimental data taken from the literature and calculated values for partial cross sections of alpha particle induced fragmentation reactions.*

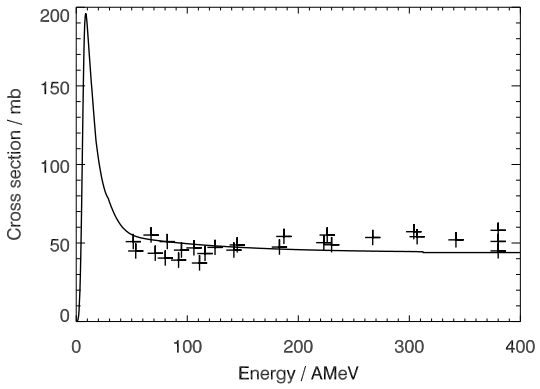

Fig. 1 *Comparison between experimental data for partial cross sections for the reaction $^{12}C(\alpha, \alpha+n)^{11}C$ (crosses) [6] [8] with calculated values.*

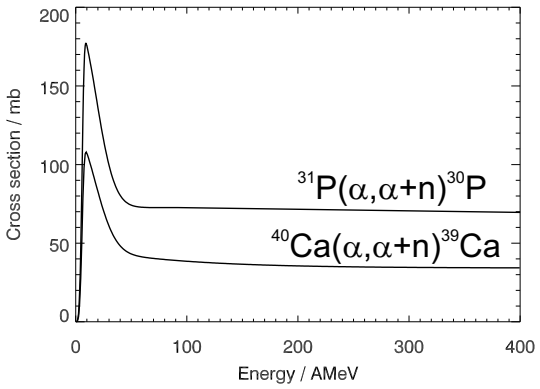

Fig. 2 *Calculated partial cross sections for the reactions $^{40}Ca(\alpha, \alpha+n)^{39}Ca$ and $^{31}P(\alpha, \alpha+n)^{30}P$*

[1] B. G. Hasch, PhD Thesis, TU Dresden (1996)
[2] C. H. Tsao, private communication (2002)
[3] R. Silberberg and C. H. Tsao, Astrophys. J. Suppl. 25 (1973) 315
[4] L. Sihver et al., Phys. Rev. C 47 (1993) 1225
[5] W. R. Webber et al., Phys. Rev. C 41 (1990) 5471
[6] J. R. Radin et al., Phys. Rev. C 9 (1974) 1718
[7] J. R. Radin, Phys. Rev. C (1970) 793
[8] M. Lindner and R. N. Osborne, Phys. Rev. 91 (1953) 1501

Hamamatsu S8550 APD Arrays for High-Resolution Scintillator Matrices Readout

B, S

M. Kapusta[1], P. Crespo, M. Moszyński[1], W. Enghardt, D. Wolski[1]

The performance of Hamamatsu S8550 avalanche photodiode (APD) arrays for scintillator matrices readout has been evaluated in order to prepare a pair of detectors to simulate a positron emission tomography (PET) system at the medical beam line of GSI Darmstadt. The S8550 device is a monolithic 8×4 pixels structure with an active area of 2.56 mm^2 for each pixel. The device allows stable operation in pulse mode at gains up to 74, with a detection efficiency of about 60 % for photons of 420 nm wavelength.

Fig. 1 presents energy spectra obtained for one pixel of S8550 using 5.9 keV X-rays as well as a 420 nm light pulser and test pulser peaks. Note that the gain of 5.9 keV X-rays is reduced because of a lower APD gain for X-rays than for light. This effect is evidently associated with the internal structure of the APD [1, 2, 3]. The measured test pulser resolution of 232 eV corresponds to an equivalent noise charge of 27 electrons.

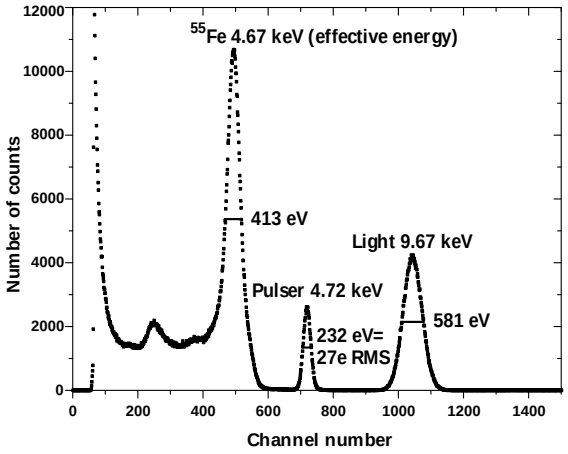

Fig. 1 *Pulse height spectra from 5.9 keV X-rays, a light pulser and a test pulser, measured for one pixel of the S8550 Hamamatsu APD array at a gain of 60. The position of the 5.9 keV X-ray peak is shifted to lower energy values, since the APD gain is lower for X-rays than for light.*

The pixel-to-pixel gain non-uniformity measured by comparing the positions of the 5.9 keV photopeak in the spectra of individual pixels was found to be less than 3.6 % at a gain of 60. Crosstalk measurements were performed in pulse mode operation by illuminating the centre of a pixel with a light spot and recording the amplitude spectra from the neighbouring pixels protected against light. The highest crosstalk between adjacent pixels was found to be 4 % at a device gain of 60. The energy resolution of 14.6 %, for the 511 keV peak from a ^{22}Na source has been recorded with a $2 \times 2 \times 10$ mm^3 LSO crystal coupled to one pixel. The number of electron-hole pairs (e-h) produced by the 511 keV photopeak absorbed in LSO is equal to 4830 ± 240 e-h/MeV.

Fig. 2 shows the coincidence time spectrum measured with precise selection of the energy windows around the full energy peak. The measured time resolution of 3.0 ± 0.2 ns FWHM obtained against BaF_2 coupled to an XP2020Q photomultiplier tube corresponds to 4.2 ± 0.3 ns FWHM for two APD-LSO detectors operating in coincidence.

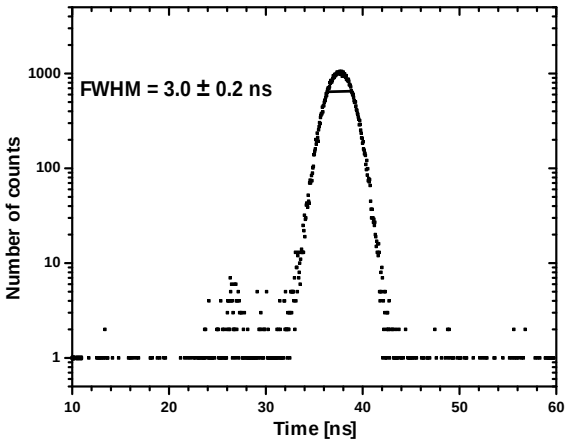

Fig. 2 *The time spectrum measured with the annihilation quanta from a ^{22}Na source.*

The Hamamatsu APD array shows good performance, but the investigations done in this work by means of the same experimental conditions and the same methods as in our previous work [3] clearly reveal that a diode layout based on the beveled structure results in superior parameters. The main disadvantage of the S8550 is its low internal gain and, consequently, its low signal-to-noise ratio. Additionally, surface effects reduce its quantum efficiency for LSO light. These drawbacks are similar to those existing with single devices produced by Hamamatsu [1], whereas the great advantage of the Hamamatsu layout is its high reliability, which has been proven in several PET applications for high resolution imaging [2].

[1] M. Moszynski, et. al., IEEE Trans. Nucl. Sci. 48 (2001) 1205
[2] B.J. Pichler, et al., IEEE Trans. Nucl. Sci. 48 (2001) 1391
[3] M. Kapusta, et al., IEEE Trans. Nucl. Sci. 49 (2002)

[1] *Soltan Institut for Nuclear Studies, 05-400 Świerk-Otwock, Poland*

Position Sensitive Photon Detectors of Lutetium Oxyorthosilicate Crystals Coupled to Avalanche Photodiode Arrays [B,S]

P. Crespo, M. Kapusta[1], K. Heidel, L. Heinrich, J. Hutsch,
J. Pawelke, M. Sobiella, D. Wolski[1], W. Enghardt, M. Moszyński[1]

In order to evaluate their performance when operated as photon detectors for in-beam ion therapy monitoring by means of positron emission tomography (PET), we have assembled and tested two position sensitive photon detectors, each consisting of 32 LSO crystals (cerium-doped Lutetium Oxyorthosilicate: Lu_2SiO_5:Ce^{3+}) coupled to a 4 x 8 pixels avalanche photodiode array (APDA). The crystals were cut from a single block delivered by CTI Inc. and their dimensions after polishing were 2 x 2 x 15 mm^3. Each crystal had all faces but one wrapped in teflon tape, with the non-covered face fixed with silicon glue to each pixel of the APDA. Fig. 1 (top) shows the assembling process, with the top of the crystals still uncovered. The whole assembly was later isolated from light with an aluminium cover. The properties of the Hamamatsu 4 x 8 APDA are described in [1]. Silicon glue was used to fix the LSO crystals to the APDA after a seven days test that compared the glue with high viscosity silicon oils (up to a viscosity factor of 2 million). During the first day the oil creeps along the teflon tape and makes it transparent to light, resulting in a decrease in light collection of 2.5 % measured after 12 hours, together with a decrease in energy resolution of 1.9 %. This effect is reduced if silicon glue is used since it solidifies in a few hours. Furthermore, by using glue crystal displacements are avoided. Before assembling the LSO crystals in the APDA their light yield homogeneity was checked with a PMT. In the horizontal position, the measured Gaussian mean was 26200 photons/MeV with 9.4 % FWHM, against 10400 photons/MeV with 22 % FWHM in the vertical position.

Once the two detector prototypes were ready we have placed them on dedicated motherboards with each pixel connected to a special purpose charge sensitive preamplifier (PA) built at the Soltan Institute for Nuclear Studies, in Warsaw, Poland. Each PA has a charge integrating output for the energy measurements and a fast output optimized for time measurements with the 40 ns decay time of LSO. Each motherboard, with its LSO/APDA detector and 32 PAs, was closed in a ventilated aluminium case offering electromagnetic protection. The timing signals of each detector were ORed with conventional electronic modules in order to operate the two detectors in coincidence.

All energy and time spectra were recorded with the hardware/software solution described in [2]. A ^{22}Na point source placed between the detectors allowed the energy spectra to be collected for all pixels (Fig. 1, middle, shows one pixel) as well as the coincidence time spectrum (Fig. 1, bottom). A non-linear least squares fit approached a Gaussian distribution with a 2^{nd} order polynomial background

to the 511 keV photopeak in the energy spectrum, as shown by the vertical dashed lines in Fig. 1 (middle). The 14.6 % FWHM energy resolution obtained is in good agreement with the mean energy resolution of 14 % FWHM obtained with the crystals vertically coupled to a XP2020Q PMT. The final gain variation between all pixels was 13 % FWHM at an APD internal gain of 70.

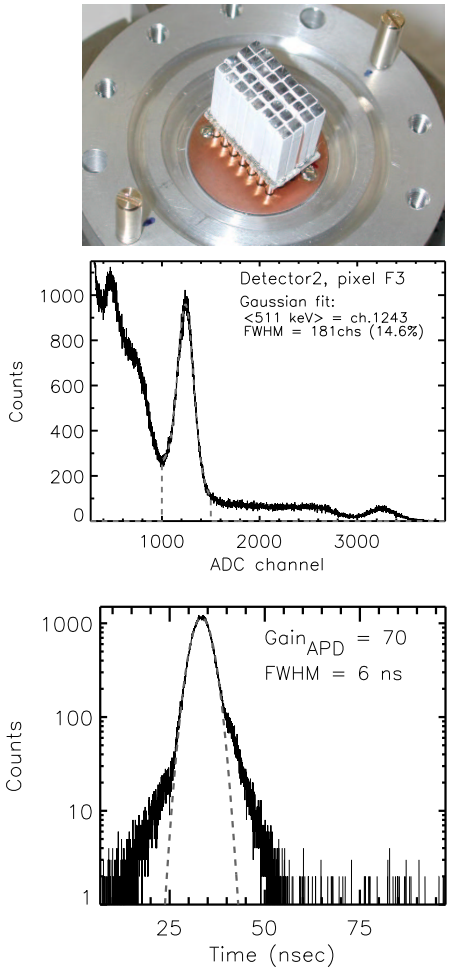

Fig. 1 *Top: Assembling of the first detector. Middle: Energy spectrum measured with a ^{22}Na source. Bottom: Coincindence time spectrum of 511 keV photons.*

[1] M. Kapusta et al., Hamamatsu S8550 APD arrays for high-resolution scintillator matrices readout, This Report, p. 80
[2] P. Crespo et al., A CAMAC data acquisition system for multi parameter measurements, This Report, p. 82

[1] *Soltan Institute for Nuclear Studies, 05-400 Otwock-Świerk, Poland.*

A CAMAC Data Acquisition System for Multi Parameter Measurements [B]

P. Crespo, J. Pawelke, W. Enghardt

We have developed a data acquisition system performing multi parameter readout of electronic modules operating under the CAMAC standard. The goal of this development was to provide a solution for the readout of two position sensitive photon detectors under study and operated in coincidence at the GSI medical beam line [1]. Each detector provides 32 energy outputs resulting in a minimum of 65 channels to be read if one considers the additional coincidence time spectrum only. Four CAMAC peak sensing ADCs are used (Phillips Scientific, model 7164), with 16 channels each. A CAMAC/GPIB crate controller (Kinetic Systems 3988) reads the ADCs and sends the data through the GPIB protocol to a GPIB/Ethernet converter (National Intruments GPIB-ENET/100). The GPIB/Ethernet converter can be accessed by any linux-running machine logged to the local network. For that, we have developed a C/C++ based application (CAGE, Camac Acquisition through GPIB and Ethernet [2]) that allows the user to control the CAMAC acquisition and to see, on-line, the spectra being collected. The GPIB/ENET driver software for linux is publicly available [3] and the control routines for the display are based on the Qt open-source package [4].

CAGE is prepared to automatically perform and display single spectrum acquisitions (rates above 40 K counts/sec achieved), two simultaneous spectra (Fig. 1), 16 spectra (Fig. 2), 64 and 66 spectra (Table 1).

When acquiring 16 spectra or less, the 65 Kword buffer (24 bit words) of the crate controller is used to maximize speed throughput by reading one ADC in the so called Q-repeat mode. In this mode, a CAMAC read function can be repeatedly executed at CAMAC bus speed ($\sim$ 1 MHz, 24 bit, parallel) and the result is stored in the buffer only when the ADC delivers a CAMAC Q-signal (valid read cycle). CAGE starts the connection protocol only when the buffer is full and, once the hand-shake between the host computer and the crate controller is performed, the full buffer is transferred in direct memory access (DMA) mode at the maximum speed of the intervening buses (8 Mbit, parallel, for the GPIB bus and 10 to 100 Mbit, serial, for the TCPIP).

If the number of spectra exceeds 16, than more than one ADC is needed as one repeated read function does not suffice. In this case, an auxilliary crate controller from Kinetic Systems (3982) is used which has two internal buffers: one for function storage and one for data, with 8 Kword each. CAGE first stores in the 3982 function buffer the CAMAC operations to be performed every time an event arrives. An Ortec ADC (811), with the slowest conversion time, sets its look-at-me (LAM) when it has finished conversion and with this starts the 3982 acquisition cycle. The 3982 runs on standalone mode, handling the arriving events and storing them in the data buffer. CAGE checks the data buffer and only reads it, in DMA mode, after it is more than half full, again optimizing the buses transfer capabilities.

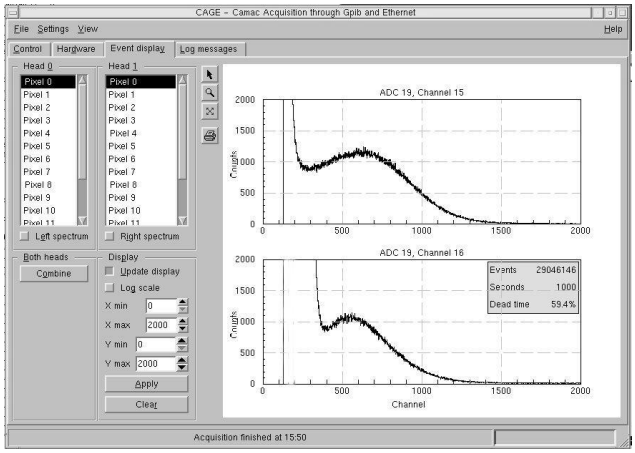

Fig. 1 *Single photoelectron spectra simultaneously acquired with two Phillips PMTs (top: XP2020Q at -2650 V, and bottom: XP3312B at -1300 V).*

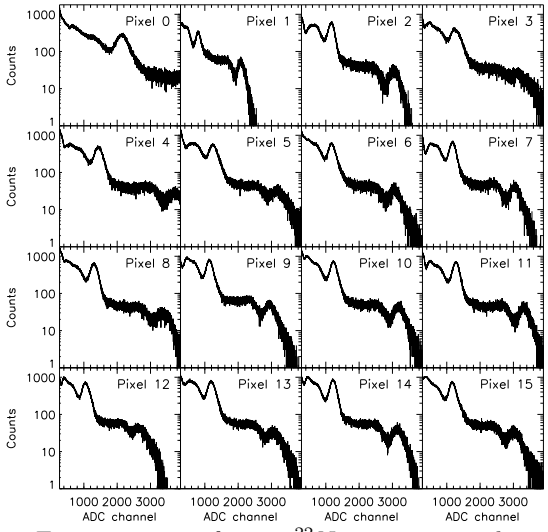

Fig. 2 *Energy spectra from a ^{22}Na source, simultaneously collected (one hour) in one of the detectors described in [1].*

Table 1 *Values obtained with a white spectrum generator.*

Output / Input	1 ch		2 chs		16 chs		32 chs		64 chs		66 chs	
	CR (cps)	DT (%)	CR (cps)	DT (%)	CR (cps)	DT (%)	CR (cps)	DT (%)	CR (cps)	DT (%)	CR (cps)	DT (%)
100 cps	98.7	1.3	98.4	1.6	96	4	92	8	87	13	86	14
1 Kcps	977	2.3	974	2.6	900	10	624	37	446	55	398	60
10 Kcps	9k	9.8	9.1k	9.5	4.4k	56	1.4k	86	745	93	611	94
100 Kcps	43k	57	29k	71	6k	94	1.6k	98.4	794	99.2	650	99.4

CR = Count Rate (counts per second), **DT** = Dead Time (%)

[1] P. Crespo et al., Position sensitive photon detectors of Lutetium Oxyorthosilicate crystals coupled to avalanche photodiode arrays, This Report, p. 81
[2] http://www.fz-rossendorf.de/FWK/MITARB/crespo/cage.html
[3] http://www.ni.com/linux/ni488dl.htm
[4] http://www.trolltech.com

A Technical Feasibility Study for a PET Therapy Monitor Combined with a Rotating Ion Beam Delivery [G]

W. Enghardt, P. Crespo, W. Bourgeois[1], A. Winter[2]

The charged hadron therapy unit that will be built on the campus of the University of Heidelberg clinics [1] will be equipped with a rotating beam delivery (gantry). An analysis of geometrical treatment configurations for skull base tumours [2] revealed that the flexibility in choosing beam portals at a gantry will provide additional benefit to the patients compared to a fixed beam delivery. It is expected that for delicate therapeutic irradiations the gantry beam delivery will be preferred rather than using a fixed beam, and, therefore, the gantry beam delivery should be equipped with an in-beam positron emission tomography (PET) system for performing in-situ monitoring of therapeutic irradiations. More than 5000 PET scans for in-situ monitoring the fractionated therapeutic irradiations of over 150 patients at the ^{12}C ion therapy facility of the Gesellschaft für Schwerionenforschung Darmstadt revealed that in-beam PET is a valuable tool for quality assurance in precision therapy with ion beams [3]. From this clinical experience the main design criteria for a novel in-beam PET scanner have been derived:

(1) Since the count rate is limited by the dose per fraction, a detector system of large solid angle and high intrisic sensitivity, i. e. detector material of superiour γ-ray registration efficiency, is required

(2) A PET-scanner to be combined with a beam delivery has to be of limited angle geometry (double head or split ring) in order to provide space for the primary beam and for the light fragments escaping the patient downbeam. As it has been shown in [4] the width of these gaps has to be minimized to reduce image degradation due to limited angle artefacts.

(3) Since the range of the primary particles as well as the position of the irradiated volume are derived from global parameters of the reconstructed β^+-activity distributions, the range and the position resolution is much better than the intrinsic spatial resolution of the PET detectors [3]. Furthermore, severe deviations from the treatment plan will cause structures with typical dimensions of several millimetres in the β^+-activity distributions [5, 6]. Thus, a PET system with a moderate spatial resolution of about 5 mm (FWHM) is sufficient for the purpose of in-beam PET therapy monitoring.

As the result of investigating the technical feasibility of several combinations of a PET-scanner with a rotating beam delivery, a configuration as depicted in Fig. 1 seems to be an optimal solution in the sense of the requirements (1) - (3) above. The integration of this tomograph into the tunnel-like treatment room is depicted in Fig. 2.

The technical features of the PET-scanner should be shortly summarized: Position sensitive block detectors of Bismuth Germanate (ECAT EXACT detectors, CPS Knoxville, TN, USA) have been proven to be reliably

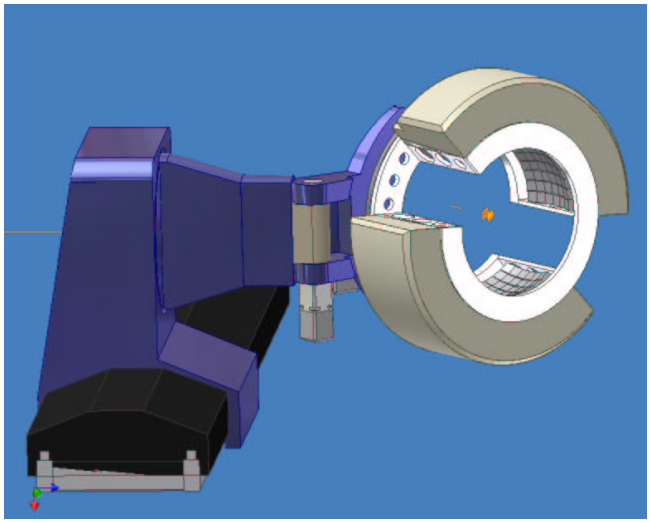

Fig. 1 *The technical concept of a positron emission tomograph for combining with a ion beam gantry*

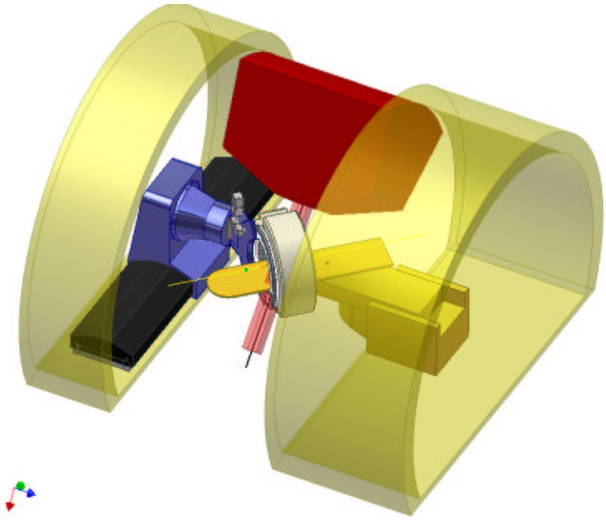

Fig. 2 *Integration of the positron emission tomograph into the treatment room. The ion beam nozzle is rotatable by 360 deg between the basements for the patient couch (right) and the PET-scanner (left). The margins of the raster scanned beam at maximal deflection (20 × 20 cm) are schematically displayed.*

operable in-beam at the GSI therapy facility. Therefore, in a first conservative approach the present feasibility study is based on this detector type. Two detector heads each comprising 96 block detectors (16 in azimutal, 6 in axial direction) form a split ring with two gaps of 32 cm width covering about 50 deg of azimutal angle, which is necessary for irradiating portals with a cross section up to 20 cm × 20 cm (Fig. 3). From the investigations of [4] it is expected that the limited angle artefacts due to

[1] *Gesellschaft für Schwerionenforschung, Darmstadt*
[2] *Institut für Energetik und Umwelt GmbH, Dresden*

gaps of that size should be negligible in imaging situations which are typical for ion therapy. The length of the axial field-of-view (FOV) of the positron camera is 31 cm. The patient port has a diameter of 74 cm and the outer diameter of the camera is 144 cm.

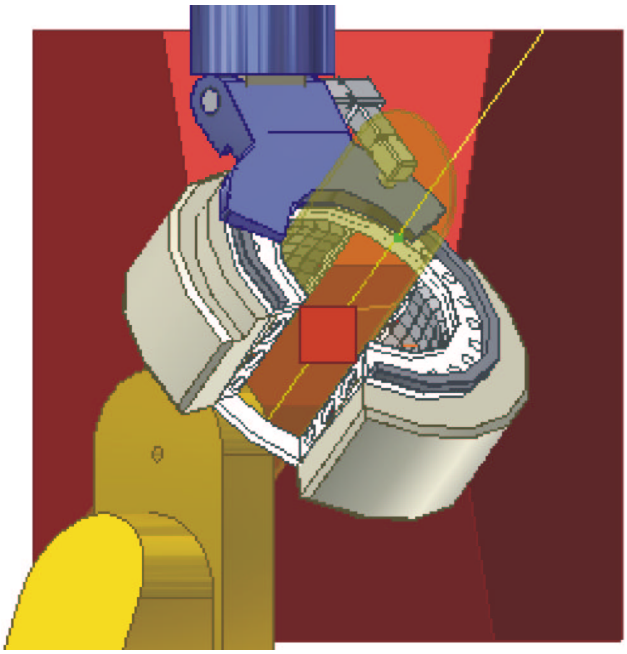

Fig. 3 *This view opposite to the beam direction proves the gaps of the split ring positron camera to be sufficiently large for irradiating portals of a maximum cross section of 20 cm × 20 cm (the square in the centre of the figure). The positions of the nozzle, the patient table and the positron camera are the same as in Fig. 2*

During imaging, i. e. during therapeutic irradiations of the patient in supine position, the positron camera covers the patient like a conventional tomograph. Since the PET-scanner has to be moved into this position after patient positioning, it is independently mounted opposite to the treatment table (Fig. 2). This arrangement allows the positron camera to be completely removed from the treatment table providing the necessary free space for patient positioning. (Fig. 4). To cover all treatment situations, the PET-gantry has to provide five degrees of freedom: *(i)* rotation of the split detector ring, *(ii)* swivelling the detector ring around a vertical excentric axis to align the scanner and the table axes, *(iii)* horizontal translation between parking and measurement positions parallel to and *(iv)* perpendicular to the longitudinal axis of the treatment tunnel, *(v)* swivelling the detector ring in the park position between the the left and right side of the pivot bearing (see Fig. 4).

A collision analysis involving the movements of the nozzle, the patient table and the positron camera for irradiation of head and neck tumours revealed a flexibility of positioning being superiour of that of a conventional therapeutic electron linear accelerator (Fig. 5).

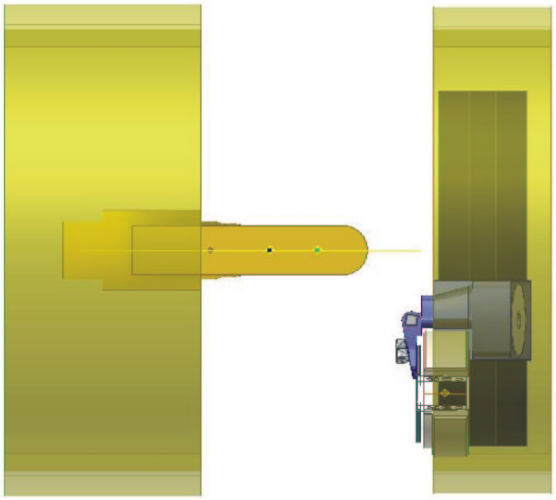

Fig. 4 *The PET scanner in the parking position (top view) provides the necessary free space for patient positioning*

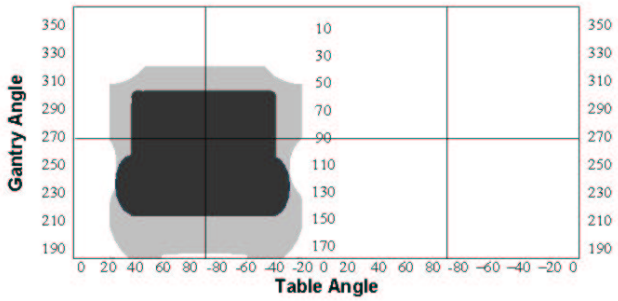

Fig. 5 *Result of the collision analysis for the combination of a gantry beam delivery and a split ring PET scanner as shown in Fig. 2. The diagram displays the gantry (nozzle) angle versus the table angle. It is separated into an inner and two outer parts; the inner part covers gantry angles between 0 and 180 deg and the outer ones between 180 and 360 deg. The light and dark grey areas in the left part of the diagram are not accessible or are unsuitable for head treatments with conventional electron linear accelerators [2] and the heavy ion beam delivery investigated here, respectively.*

[1] Heavy Ion Therapy Unit at the University of Heidelberg Clinics, Universitätsbauamt Heidelberg, 2002

[2] O. Jäkel, J. Debus, Phys. Med. Biol. 45 (2000) 1229

[3] K. Parodi, W. Enghardt, T. Haberer, Phys. Med. Biol. 47 (2002) 21

[4] P. Crespo, K. Lauckner, W. Enghardt, FZ Rossendorf, Wiss.-Tech. Ber. FZR-341 (2002) 104

[5] K. Parodi, W. Enghardt, Wiss.-Tech. Ber. FZR-341 (2002) 98

[6] W. Enghardt et al. Wiss.-Tech. Ber. FZR-271 (2000) 89